Article

Computational Fluid Dynamic Investigation of Local Flow-Field Conditions in Lab Polymer Electrolyte Membrane Fuel Cells to Identify Degradation Stressors and Performance Enhancers

Margherita Bulgarini, Augusto Della Torre *, Andrea Baricci, Amedeo Grimaldi, Luca Marocco, Riccardo Mereu, Gianluca Montenegro and Angelo Onorati

Department of Energy, Politecnico di Milano, 20156 Milan, Italy; margherita.bulgarini@polimi.it (M.B.)
* Correspondence: augusto.dellatorre@polimi.it; Tel.: +39-02-2399-8631

Abstract: The use of polymer electrolyte membrane (PEM) fuel cells as an alternative to internal combustion engines can significantly contribute to the decarbonization of the transport sector, especially for heavy-duty applications. However, degradation is still an issue for this type of component, affecting their durability and performance. In this scenario, a detailed analysis of the anodic and cathodic distributors' flow-field geometry may help to identify some local stressors that trigger the degradation mechanism, such as local hot spots and reactants not having a uniform distribution. A computational fluid dynamic (CFD) methodology is able to provide a volumetric description of a PEM fuel cell so it can be a useful tool to better understand the physical phenomena that govern the component operations. In this work, the open-source simulation library *openFuelCell2* is adopted for a detailed analysis of two different PEM fuel cells characterized by standard distributor geometries, namely a parallel channel geometry and a serpentine configuration. The library, based on the Open-FOAM code, has been extended with a novel implementation accounting for the catalytic activity reduction due to the platinum oxide (PtOx) formation occurring under certain particular conditions. The adopted methodology is firstly validated resorting to experimental data acquired for the two different fuel cell configurations. The analysis highlights that the PtOx formation leads to a reduction in the fuel cell performance reaching up to 60–80% when operating at high voltages. Then, the effect of the distributor geometries on the component performance is investigated by resorting to in-plane and through-plane physical quantity distribution, such as reactant concentration, pressure or velocity fields. While the parallel flow channel configuration shows some diffusion losses under the rib, the serpentine channel geometry configuration can achieve some local performance peaks thanks to the convective flow in the gas diffusion layer (GDL) driven by local pressure gradients. Furthermore, the local enhancement in terms of higher current density under the rib is associated with an effective heat removal due to the high thermal capacity of the bipolar plate, avoiding the generation of local hot spots.

Keywords: fuel cell; CFD analysis; distributor geometry; platinum oxidation; degradation

1. Introduction

The polymer electrolyte membrane fuel cell (PEMFC) is a promising zero-emission solution for power generation. In particular, it can be used in the mobility sector, especially for heavy-duty applications, in order to cope with the challenging goal of zero CO_2 emissions before 2035. In fact, this component can electrochemically convert hydrogen and oxygen into water producing electrical energy, without any pollutant emissions. Moreover, PEMFCs are characterized by low operating temperatures, high efficiency and low noise. However, lifespan and durability are still an issue for this type of component that is exposed to different degradation mechanisms during its operation [1].

Water management is a fundamental aspect to be considered when speaking about PEMFC degradation and performance optimization [2]. Humidity and water content

depend on the amount of vapor produced during the electrochemical reactions, that may condense into water, and on the level of relative humidity at the anode and cathode channel inlet. The control of these two parameters is fundamental during the fuel cell design and optimization processes. In fact, a low water content may lead to membrane dehydration, resulting in a decrease in the ionic conductivity together with the formation of local hot spots, which can damage the component. On the other hand, membrane flooding may occur for a high water content and it severely reduces the reactant supply from the flow-field channels to the catalyst layer surfaces, thus reducing the cell performance. Porous media materials have a strong impact on obtaining proper membrane hydration. Moydien et al. [3] compared conventional carbon with a titanium fiber gas diffusion layer (GDL). The second one showed higher performance due to a higher air permeability. Xu et al. [4] investigated the liquid saturation behavior for three different commercial GDL materials in order to analyze the effect of GDL on cell performance and provide guidelines for the selection of the materials. The porous media composition also determines the GDL hydrophobic behavior. It is required for a proper water management in order to avoid a pore blockage effect due to the condensed water. As shown by Chen et al. [5], the Polytetrafluoroethylene (PFTE) content is a key parameter to determine not only the GDL thermal and electrical conductivity, but also its tendency to evacuate water toward the flow-field channels. Wang et al. [6] proposed a strategy to optimize the GDL hydrophobicity through the modification of the surface roughness and fiber diameter using a high-temperature sintering process after a hydrothermal deposition, thus increasing the fuel cell performance.

Not only the material properties but also the geometrical features of the porous media are fundamental parameters for water management. Liu et al. [7] investigated the effect of GDL thickness on the diffusion of reactants and thus on the PEMFC performance. This parameter must be chosen as a function of the rib width as a trade-off between gas transport and water removal capacity. The presence of cracks changes the water intrusion path in the GDL structure. It provokes a variation in the water intrusion rate and liquid storage volume within the GDL and thus a variation of water management too, as shown by Dong et al. [8]. Geometrical features have an impact also when focusing on the micro-scale. In fact, pore structure and micro-structural characteristics play an important role in the diffusion of reactants towards the active sites. Xiao et al. [9] evaluated the effect of many micro-structural characteristics on PEMFC performance such as fiber diameter and orientation, porosity, GDL thickness or PTFE content. It was found that porosity has a higher impact degree on gas diffusion and heat conduction. Yin et al. [10] proposed a microelliptical groove GDL structure that is able to increase the diffusion of reactants and water evacuation from active sites. GDL micro-structure strongly affects not only water management but electrical and thermal conductivity too. Ye et al. [11] analyzed the effect of GDL micro-structure on different micro-conduction mechanisms, highlighting the dependence of fiber density and diameter or binder aggregation on the conduction performance of GDL. Moreover, the heterogeneous porosity distribution has a strong impact on the GDL thermal conductivity as found by Yablecki et al. [12].

The analysis of new architectures can also provide solutions to water management issues. Cheng et al. [13] examined the behavior of water transport plates that utilize the differential pressure between the cathode and coolant chamber to enable passive water management. This approach does not increase parasitic power, thereby enhancing the liquid distribution and improving the cell performance.

The geometrical characteristics of the reactant flow-field distributor have a significant effect on PEMFC performance and degradation [14]. Different types of flow fields have been studied to optimize various aspects as pressure drops, membrane hydration or reactant distribution across the active area [15]. The flow in the distributor can be convection-dominated, as for a serpentine channel geometry, or diffusion-dominated, as for the parallel channel configuration. The parallel flow-field configuration guarantees a low pressure drop considering a laminar regime [16]. However, little uneven flow distribution can lead

to uneven heating and local starvation. To increase the flow uniformity, tapered channels or baffles may be used. Saco et al. [17] numerically investigated the effect of a straight zig-zag flow channel on performance. Higher reactant consumption and better water removal rate in the channels together with better water distribution in the electrolyte result in a higher power output compared to a simple parallel channel configuration. Shen et al. [18] studied a straight channel with single and double side blockage to enhance charge and mass transport, but pressure losses increased. Constriction and enlargement cross-sections were analyzed by Brakni et al. [19] to investigate their effect on PEMFC performance. The cross-section reduction increased fluid velocity, thus improving the flow distribution with higher pressure losses. Moreover, a better temperature distribution, higher oxygen consumption, improved membrane humidification and water removal were observed, thus in the end increasing PEMFC performance. Zheng et al. [20] investigated the effect of bio-inspired sinusoidally waved flow fields, which allow a reduction in the parasitic power, improving the reactant distribution and water management with respect to a wave-shaped structure. Toghyani et al. [21] achieved an increase in oxygen diffusivity within the media using a bean-shaped flow field compared to a parallel flow channel configuration, thereby improving the cell performance.

A serpentine flow channel configuration allows a more uniform distribution of reactants and an effective cooling of the active area, but also higher pressure drops than parallel flow channels due to the higher tortuosity of the flow field. Under the U-shaped corners, some problems arise, such as a decrease in reactant concentrations or poor water management. The use of rounded corners or wider channels can mitigate them [22]. Another solution is to arrange the serpentine flow field in series and parallel flow paths [23]. The cell performance can be improved with respect to a single channel serpentine geometry by increasing the segment number or the channel path number in each segment, thanks to the reactant transport under the ribs and secondary flow in the channel. Alizadeh et al. [24] proposed a cascade-type serpentine geometry, which produced a uniform current density and a good water management. Abdulla et al. [25] analyzed the performance of an enhanced cross-flow split serpentine flow field, obtaining higher performance compared to a parallel serpentine design.

Not only two-dimensional type flow fields, but also three-dimensional regions such as metal foam, fine-mesh or wire-mesh flow fields with porous structure have been investigated in the literature [26]. These types of structures are able to significantly improve mass transfer, creating forced convective flow and thus increasing PEMFC performance with respect to a two-dimensional type flow field [27]. Complex three-dimensional flow-field structures can be obtained thanks to the metal 3D printing process, enhancing the convection effect in the through-plane direction, increasing water management and reactant diffusion, thus obtaining higher performance [27].

The different physical phenomena occurring in a PEMFC device are many and complex, and their deep understanding is required in order to investigate degradation and enhance performance. Computational Fluid Dynamics (CFD) can be a valuable tool for a better understanding of the PEMFC operations thanks to a volumetric discretization of the component [28]. Both in-plane and through-plane distributions of the most significant fields can be computed, such as water content or reactant concentration [29]. In this work, an open-source simulation library based on the OpenFOAM code [30] has been applied to simulate two different PEMFC components. In particular, a parallel flow channel configuration and a serpentine distributor geometry are analyzed. The physical mechanisms which determine the overall component performance are investigated in detail and compared among the two configurations. In order to enhance the predictivity of the model, the simulation library has been extended with the implementation of a kinetic mechanism accounting for the oxidation of the platinum catalyst under particular conditions. This phenomenon, occurring at low current density and high voltage, is responsible for the reduction in the activity on the electrochemical reactions, leading to a reduction in the cell

performance [31,32]. The model has been validated on both the configurations by means of experimental data acquired for the analyzed components.

This paper is structured as follows. Firstly, an overview of the adopted methodology is presented, including a detailed discussion of the electrochemistry models used, focusing on the implementation of the platinum oxide (PtOx) formation and its effect on oxygen reduction reaction (ORR). Then, the two PEMFC configurations studied in this work are presented. A validation of the CFD methodology is carried out on these two devices in terms of the polarization curve, highlighting the effect of PtOx on their performance. A detailed analysis of the in-plane and through-plane distributions of the most significant fields is carried out in order to provide a local insight into the transport and electrochemical phenomena. The influence of the distributor geometry on the local operating conditions of the membrane is investigated, showing how the design of the channel arrangement can enhance the convective transport of reactants through the GDL.

2. Methodology

In this section, the CFD methodology applied in this work is described, providing an overview of the base model adopted and highlighting the specific contribution implemented to improve the description of the electrochemical phenomena.

2.1. Simulation Model

The PEMFC components are modeled in the OpenFOAM environment using the open-source *openFuelCell2* library developed by Zhang et al. [33]. This library can be used for the modeling of different electrochemical devices such as low and high temperature fuel cells or electrolyzers. It is based on a multi-region and multi-physics approach to properly account for the different phenomena occurring in an electrochemical device, such as fluid flow, heat and mass transfer, reactant species, and charge transfer and electrochemical reactions.

The CFD framework is based on the adoption of different computational grids. On the global mesh, also called the "parent mesh", the energy conservation equation is solved. Different "child meshes" are then used to properly solve the specific governing equations that describe the major transport phenomena in the different PEMFC components, namely flow fields, MEAs (which consist of the membrane and the two catalyst layers) and bipolar plates (Figure 1). The methodology considers three different regions—solid, fluid and electric—on which different physics are solved based on the following assumptions:

- A laminar regime is assumed for all gas and liquid flows.
- Both gas and liquid phases are assumed to be incompressible and gas mixtures follow the ideal gas law.
- Multi-component species transfer is described using Fick's law.
- The porous media are assumed to be isotropic so their properties are considered as homogeneous.
- The membrane is considered to be impermeable to gases; thus, only crossover of water is modeled in the membrane electrode assembly (MEA).
- Water produced from the electrochemical reactions is considered to be liquid when the operating temperature is lower than 100 °C.
- The amount of gases dissolved in liquid water is neglected.
- The amount of water dispersed in the gas channel is considered as if composed of spherical bubbles.
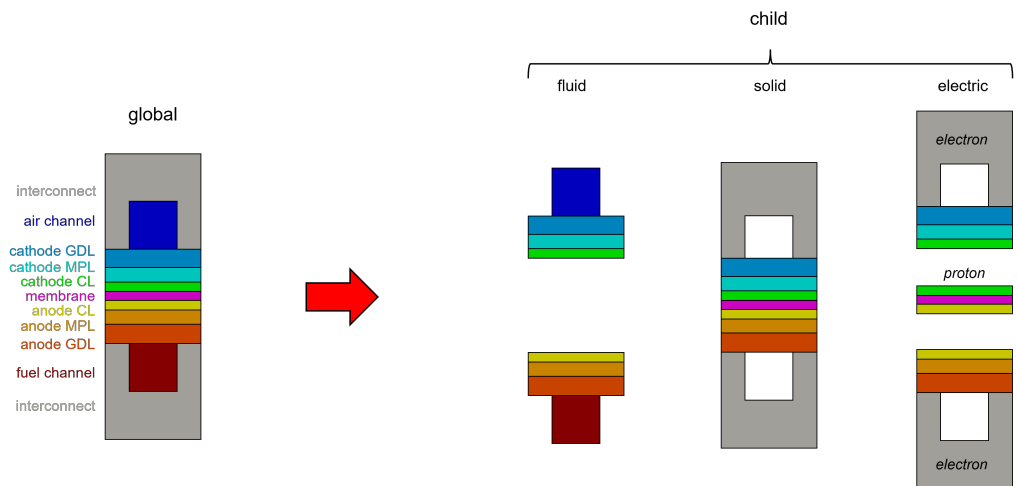
Figure 1. Overview of the global and child meshes adopted for the modeling of a generic fuel cell.

2.2. Modeling of the Fluid Region

In the fluid region, continuity and momentum equations are solved in the flow channels and a multi-phase flow is modeled. So, water can exist in both liquid and vapor phases. A conditionally averaged continuity and momentum equations are solved [34]. To compute the water evaporation and condensation rates, the temperature at the interface among the two phases, indicated as T_{int}, is assumed and the corresponding transferred species i interfacial mass fraction $Y_{int,i}$ is computed as follows:

$$Y_{int,i} = \frac{M_i}{M_{mix}} \frac{p_{sat}(T_{int})}{p_i} \tag{1}$$

where M_{mix} isthe molar mass of the mixture, p_{sat} is the saturation pressure of the liquid dispersed in the gas phase and p_i is the partial pressure of the gas. The mass transfer rate m''_{21} is expressed as follows:

$$m''_{21} = \frac{\Gamma}{\delta} \frac{Y_1 - Y_{int}}{Y_{int} - 1} \tag{2}$$

where Γ is the thermal diffusivity and δ is the distance between the interface and the phase bulk. The energy balance between the two phases is expressed as follows:

$$k_2 \frac{T_{int} - T_2}{\delta_2} + k_1 \frac{T_{int} - T_1}{\delta_1} = m''_{21} h_{21} \tag{3}$$

where k and h are the thermal conductivity and enthalpy of each phase, respectively. Then, from Equation (3), T_{int} can be computed through the use of a Newton's method algorithm.

Unlike in the flow channels, when porous media are accounted for, the momentum equation is solved considering a Darcy-modified Navier–Stokes equation [35]:

$$\frac{\partial}{\partial t}(\rho_\phi \alpha_\phi \mathbf{U}_\phi) + \nabla \cdot (\rho_\phi \alpha_\phi \mathbf{U}_\phi \mathbf{U}_\phi) = -\alpha_\phi \nabla p_\phi + \nabla \cdot (\alpha_\phi \mu_\phi \nabla \mathbf{U}_\phi) + \alpha_\phi \rho_\phi \mathbf{g} + \mathbf{M}_\phi + \alpha_\phi S_{Darcy,\phi} \tag{4}$$

where $\mathbf{M}_\phi$ is the interface momentum transfer and $S_{Darcy,\phi}$ is the porous media resistance. It is computed as follows:

$$S_{Darcy,\phi} = -\frac{\alpha_\phi \mathbf{U}_\phi \mu_\phi}{K \cdot K_{r,\phi}} \tag{5}$$

where K is the absolute permeability and $K_{r,\phi}$ is the relative permeability of each phase. It is computed according to $K_{r,\phi} = \alpha_\phi^3$ [36]. Water can move through the porous media due to the capillary pressure acting as the driving force. It is computed according to the following:

$$p_c = \frac{\sigma \cos \theta}{\sqrt{\frac{K}{\epsilon}}} J(\alpha_l) \tag{6}$$

where σ represents the surface tension between the liquid and gas phases, θ and ϵ are the contact angle and porosity of the porous material, respectively, and $J(\alpha_l)$ is the Leverett J function [37,38]. It is computed as follows:

$$J = \begin{cases} 1.417(1 - \alpha_l) - 2.120(1 - \alpha_l)^2 + 1.263(1 - \alpha)^3 & \text{if } \theta < 90 \\ 1.417\alpha_l - 2.120\alpha_l^2 + 1.263\alpha_l^3 & \text{if } \theta > 90 \end{cases} \tag{7}$$

So, the phase pressure p_ϕ is equal for gas and liquid phases in the flow channels, while in the porous electrodes a capillarity pressure p_c is detected. This is computed as the difference between the gas pressure p_g and the liquid pressure p_l:

$$p_c = p_g - p_l \tag{8}$$

The diffusion of different species in the gas phase within the porous media is described by the following governing equation:

$$\frac{\partial}{\partial t}(\rho_\phi \alpha_\phi Y_i) + \nabla(\rho_\phi \alpha_\phi \mathbf{U}_\phi Y_i) = \nabla \cdot (\alpha_\phi \rho_\phi D_i^{eff} \nabla Y_i) + \alpha_\phi R_i \tag{9}$$

where the subscript i refers to the different species components, Y is the mass fraction and R is the species mass source/sink accounting for the electrochemical reactions. D^{eff} represents the effective species diffusion coefficient and it is computed starting from the model developed by Fuller et al. [39]. Then, the effect of tortuosity, porosity and water condensation are considered to properly take into account the diffusivity decrease. The diffusion of gases in the liquid phase is instead assumed to be negligible.

2.3. Modeling of the Solid Region

The solid region includes the bipolar plates, diffusion layers and MEA, collecting all the information related to the thermal properties of the materials which constitute the cell. In this region, no governing equations are solved explicitly, as the energy balance and the heat transfer among the sub-domains are considered at the level of the parent domain. Moreover, the solid region could be exploited, in future works, for the description of the mechanical functionality of the assembly, eventually enabling, with a specific implementation, the solution of mechanical stress.

2.4. Modeling of the Electric Region

The electric region overlies the fluid and solid regions, corresponding to the porous media and ribs, respectively. The H$^+$ ion transfer process through the catalyst layers, the membrane and the ribs is modeled in this region. Thus, Ohm's law is considered to guarantee the conservation of the electronic and protonic charges:

$$\nabla \cdot (\sigma_E \nabla \phi_E) = J_E \tag{10}$$

$$\nabla \cdot (\sigma_I \nabla \phi_I) = J_I \tag{11}$$

ϕ and σ are the electronic or ionic potential and conductivity, respectively, while J indicates the source/sink of charge due to the electrochemical reactions. The subscripts E and I indicate electronic and ionic quantities, respectively. The ionic conductivity σ_0 is

computed both in the membrane and in the porous electrodes using the relation developed by Springer et al. [40]. This depends both on water content and temperature as follows:

$$\sigma_0 = \begin{cases} (0.514\lambda - 0.326)\exp(1268(\frac{1}{303} - \frac{1}{T})) & \text{if } \lambda \geq 1 \\ 0.1879\lambda \exp(1268(\frac{1}{303} - \frac{1}{T})) & \text{if } \lambda < 1 \end{cases} \quad (12)$$

To properly take into account the volumetric fraction of Nafion ϵ_{Naf} in the catalyst layers, the ionic conductivity is then corrected [41]:

$$\sigma_I = \xi \cdot \sigma_0 \cdot \epsilon_{Naf}^{1.5} \quad (13)$$

In this work, an additional calibration coefficient $\xi = 3$ is included in the computational model. This may be due to the fact that in the adopted methodology the porous media are assumed to be homogeneous, while their properties are anisotropic. In particular, the in-plane direction is favored compared to the through-plane one for thermal and electrical conductivity.

In the electric region, in addition to the ion transfer process, the water transfer through the membrane is modeled and solved. In fact, the membrane selectively allows the crossover of water in the λ phase only, while it is considered as impermeable to gaseous reactants and products. This transport phenomenon is modeled accounting for different transport mechanisms, namely the electro-osmotic drag (EOD) and the back diffusion. With the first one, water is transported with protons from anode to cathode, while the second one is caused by a concentration gradient across the membrane, so water moves from cathode to anode. The governing equation for this non-equilibrium transport phenomenon can be written as follows:

$$\frac{\rho_m}{EW}\frac{\partial \lambda}{\partial t} + \nabla(\frac{i_P}{F}n_d) = \frac{\rho_m}{EW}\nabla \cdot (D_m^{eff}\nabla\lambda) + R_\lambda \quad (14)$$

where ρ_m is the density of the dry membrane, EW is the membrane equivalent weight, λ indicates the molar concentration water content and i_P is the ionic current density. The EOD coefficient is indicated as n_d and it is calculated according to [40]:

$$n_d = \frac{2.5\lambda}{22} \quad (15)$$

D_m^{eff} is the effective water diffusion in the membrane and it is computed as follows:

$$D_m^{eff} = \begin{cases} 3.1 \cdot 10^{-7}\lambda(e^{0.28\lambda} - 1)e^{\frac{-2436}{T}} & \text{for } 0 < \lambda < 3 \\ 4.2 \cdot 10^{-8}\lambda(161e^{-\lambda} + 1)e^{\frac{-2436}{T}} & \text{for } 3 \leq \lambda \leq 17 \end{cases} \quad (16)$$

To properly account for water desorption/adsorption in the membrane, the source/sink term R_λ is used. It is function of the water content λ and it is computed according to the following:

$$R_\lambda = \xi \frac{\rho_m}{EW}(\lambda_{eq} - \lambda) \quad (17)$$

where ξ is considered to be a constant parameter and equal to 1.2. λ_{eq} is the equilibrium water content in the membrane. It is function of the water activity a:

$$a = \frac{x_v p}{p_{sat}} \quad (18)$$

and it is computed according to [40] as follows:

$$\lambda_{eq} = \begin{cases} 0.043 + 17.81a - 39.85a^2 + 36a^3 & \text{for } 0 < a \leq 1 \\ 14 + 1.4(a - 1) & \text{for } 1 \leq a \leq 3 \end{cases} \quad (19)$$

Implementation of a Kinetic Mechanism Accounting for Pt Oxide Formation

To properly model the PEM fuel cell operating conditions, it is important to take into consideration the formation of oxide species on platinum nanoparticles, a phenomenon that negatively impacts fuel cell performance. PtOx form on the surface of the electrocatalyst nanoparticles at electrode potential values typical of the oxygen reduction reaction (>0.8 V vs. RHE). Platinum oxides, which chemistry is not fully understood in the literature under real-world conditions, partially covers the active sites, thus inhibiting the oxygen reduction reaction (ORR) at the cathodic electrode. A decrease in ORR activity is the obtained effect at the device scale, resulting in a cell voltage drop. A simplified model to simulate PtOx formation is proposed by Jomori et al. [42]. It is assumed that the process is governed by a Butler–Volmer equation:

$$\frac{\partial \theta_{PtOx}}{\partial t} = k_{PtOx}\left((1 - \theta_{PtOx})\exp\left(\frac{\alpha'_a F}{RT}\eta_{PtOx}\right) - \theta_{PtOx}\exp\left(\frac{-\alpha'_c F}{RT}\eta_{PtOx}\right)\right) \tag{20}$$

$$\eta_{PtOx} = -\Phi_c + \Phi_{ion} + U_{PtOx} \tag{21}$$

where k_{PtOx} is the PtOx formation reaction rate, α'_c and α'_a are the cathodic and anodic transfer coefficients for PtOx formation, Φ_c and Φ_{ion} are the potential in the carbon and ionomer phases, respectively, and U_{PtOx} is the PtOx equilibrium potential. Thus, θ_{PtOx}, the PtOx coverage ratio, is computed as follows:

$$\theta_{PtOx} = \frac{\exp\left(\frac{\alpha'_a F}{RT}\eta_{PtOx}\right)}{\exp\left(\frac{\alpha'_a F}{RT}\eta_{PtOx}\right) + \exp\left(\frac{-\alpha'_c F}{RT}\eta_{PtOx}\right)} \tag{22}$$

θ_{PtOx} is accounted for in the ORR kinetic expression according to [43]:

$$j_{cat} = i_{0,cat}(1 - \theta_{PtOx})\exp\left(\frac{-\omega\theta_{PtOx}}{R_g T}\right)\prod_i\left(\frac{C_i}{C_{ref}}\right)^{\xi}\exp\left(\frac{-\alpha_{cat}^{cat} F\eta_{cat}}{R_g T}\right) \tag{23}$$

while the hydrogen oxidation reaction (HOR) kinetic is computed using the Butler–Volmer equation and the effect of water saturation on the anodic electrochemical reaction rate is neglected according to [44]. Thus, the HOR results to be as follows:

$$j_{an} = i_{0.an}\prod_i\left(\frac{C_i}{C_{ref}}\right)^{\xi}\left[\exp\left(\frac{-\alpha_{an}^{an} F\eta_{an}}{R_g T}\right) - \exp\left(\frac{-\alpha_{cat}^{an} F\eta_{an}}{R_g T}\right)\right] \tag{24}$$

where i_0 is the exchange current density, θ_{PtOx} is the PtOx coverage ratio, ω is the Temkin isotherm energy parameter and F is the Faraday's constant. C_i and C_{ref} are the reactant and its corresponding reference concentration, respectively, α represents the transfer coefficient and η is the activation overpotential for the anodic and cathodic reactions. They are computed as follows:

$$\eta_{an} = \varphi_E - \varphi_I - E_{Nernst,an} \tag{25}$$

$$\eta_{cat} = \varphi_E - \varphi_I - E_{Nernst,cat} \tag{26}$$

where E_{Nernst} is the Nernst potential and it is computed as follows:

$$E_{Nernst} = E_0 - \frac{RT}{nF}\ln\frac{\prod_j(P_j)^{b_j}}{\prod_i(R_i)^{a_i}} \tag{27}$$

where the exponents a_i and b_j are the stoichiometric coefficients of the reactants R_j and products P_j, respectively. Finally, the computed electrochemical reaction rates are substituted in Equations (10) and (11) and it results, for the anode side, in the following:

$$\begin{cases} J_E = j_{an} \\ J_I = -j_{an} \end{cases} \tag{28}$$

while, for the cathode side,

$$\begin{cases} J_E = -j_{cat} \\ J_I = j_{cat} \end{cases} \tag{29}$$

3. Case Study

Two different PEM fuel cells are considered to validate the methodology and demonstrate the physical insight obtainable through detailed CFD simulations. The first configuration features a parallel flow channel layout, while the second one utilizes a serpentine channel geometry. The geometric characteristics and testing operating conditions used in the experimental campaigns are described in the following sections.

3.1. Parallel Channel Geometry

The parallel channel geometry configuration consists of zero-gradient PEMFC hardware (Figure 2). It has been developed and tested at the Politecnico di Milano by the *MRT Fuel Cell & Battery Lab* [45]. The cell hardware has been realized to minimize the influence from testing hardware on the results of durability tests and performance. Indeed, with this particular cell architecture, it is possible to maintain homogeneous operative conditions along the MEA. Thus, it results in uniform distributions of pressure, temperature and reactant gas composition across the channel length. In this way, the anodic and cathodic channel longitudinal variation in the operating condition is almost negligible. On the other hand, their major variation is found in the through-plane direction, so across the porous media between the reactant channel and the membrane.
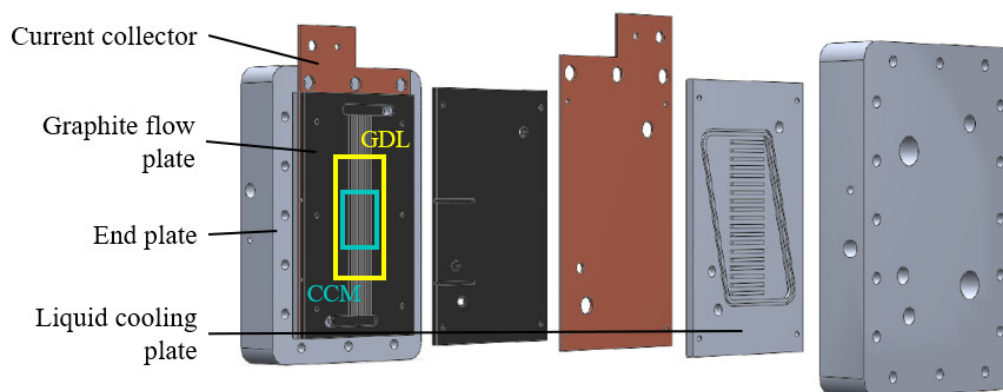
Figure 2. Zero-gradient cell hardware configuration.

The component is characterized by a parallel flow channel configuration. It is constituted by 24 and 25 channels on the cathode and anode sides, respectively. The latter are characterized by a square cross-section (0.3 mm × 0.3 mm) with a rib thickness of 0.55 mm, while the former by a rectangular cross-section (0.4 mm × 0.6 mm) and a rib thickness of 0.25 mm. The active surface, defined by Mylar® sub-gaskets, is characterized by a width of 20 mm and a length of 50 mm, resulting in an extension of 10 cm^2. The properties of the commercial catalyst coated membrane (CCM), in particular the dimensions of each component, are listed in Table 1. The platinum loading at anode and cathode is 0.08 and 0.4 mg cm^2, respectively. The commercial GDL is Freudenberg H14CX483. Their material properties are instead summed up in Table 2.

Table 1. Dimensions of the MEA components in the parallel channel geometry configuration [46].

	MEM	**CCL**	**ACL**	**MPL**	**GDL**
Thickness/mm	0.015	0.01	0.005	0.022	0.117

Table 2. Material properties of parallel channel geometry configuration [47,48].

|	ρ [kg/m^3]	ϵ	k [W/mK]	σ [S/m]	c_p [J/kgK]
MEM	1980		0.22	5×10^{-4}	1000
GDL	2200	0.65	0.16	374	720
MPL	2260	0.44	0.16	117	870
CL	2170	0.4	0.2	200	720
Collector	2260		20	10,000	720

The experimental campaign on the parallel flow-field geometry has been carried out using high stoichiometric ratios. They are made equal to 8 and 10 on the cathode and anode sides, respectively, resulting in a high excess of reactants on both sides of the cell. In fact, a parallel channel configuration allows minimizing the pressure losses, but the water management and gas distribution are not optimized. Then, using high stoichiometric factors can help to minimize these drawbacks, homogenizing the gas and water distributions. The cathode and anode channel lengths are, respectively, equal to 123.5 mm and 96 mm. Their length is significantly greater than that of the MEA, allowing the flow to develop and preheat before reaching the porous media. The polarization curve is experimentally measured considering the operating conditions listed in Table 3.

Table 3. Experimental test operating conditions for parallel channel geometry.

Anode inlet relative humidity [%]	100
Cathode inlet relative humidity [%]	100
Hydrogen inlet mole fraction [-]	0.810
Oxygen inlet mole fraction [-]	0.209
Cell temperature [K]	353.15
Absolute anode pressure [Pa]	$2.5 \cdot 10^5$
Absolute cathode pressure [Pa]	$2.3 \cdot 10^5$
Hydrogen stoichiometry	8
Oxygen stoichiometry	10

3.2. Serpentine Channel Geometry

The serpentine channel geometry configuration Figure 3 has been experimentally tested in [49]. Its geometrical and physical characteristics, together with the measured experimental data, have been collected from [50]. The component is characterized by a serpentine flow field composed of three identical squared channels, for both the cathode and anode sides, characterized by a 1 mm side. The reactant gas flow direction is a co-flow configuration. The fuel cell presents a squared active area of 17.64 cm^2, with a side length of the bipolar plates of 42 mm. It is constituted of a 42 μm thick GORE CCM, consisting of a SELECT$^®$ membrane (MEM), 18 μm thick, and two catalyst layers (CL), 12 μm each. The Freudenberg H2315 CX165 GDL is made of non-woven carbon cloth with a PTFE loading of 0% and a micro porous layer (MPL) with PFTE loading of 40%. The dimensions of each component constituting the PEMFC are listed in Table 4, while their material properties are summarized in Table 5.
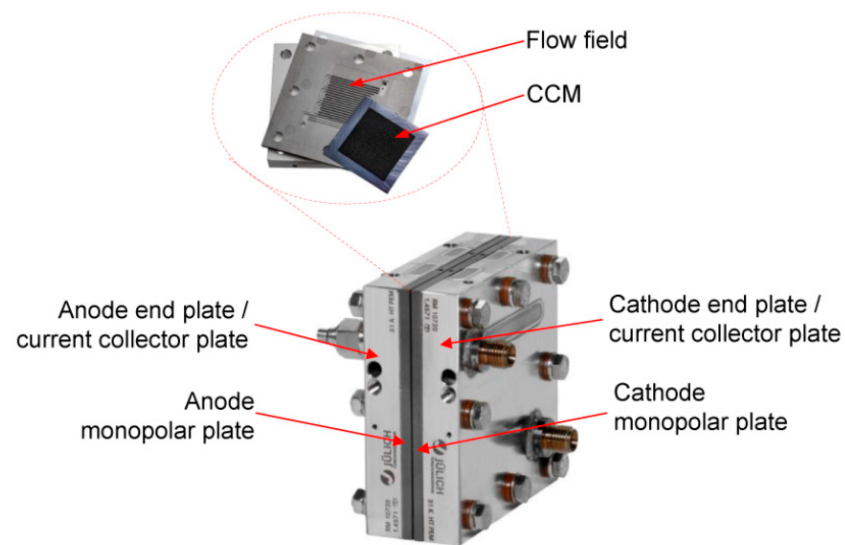
Figure 3. Serpentine cell hardware configuration [49].

Table 4. Dimensions of the MEA components in the serpentine channel geometry configuration.

	MEM	CCL	ACL	MPL	GDL	Monopolar Plate
Thickness/mm	0.018	0.012	0.012	0.039	0.208	3

Table 5. Material properties of serpentine channel geometry configuration.

	ρ [kg/m^3]	ϵ	k [W/mK]	σ [S/m]	c_p [J/kgK]
MEM	1970		0.22	1×10^{-4}	1000
GDL	1800	0.5	100	8000	709
Collector	2266		100	10,000	711

The serpentine fuel cell component operates at 70 °C with inlet relative humidity made equal to 90%, for both the anode and cathode sides. Lower stoichiometric factors with respect to the parallel channel configuration are used in this case, made equal to 1.2 and 2.5 on the anode and cathode sides, respectively. The operating conditions adopted for the measurement of the experimental polarization curve are summarized in Table 6.

Table 6. Experimental test operating conditions for serpentine channel geometry.

| Anode inlet relative humidity [%]	90
Cathode inlet relative humidity [%]	90
Hydrogen inlet mole fraction [-]	0.722
Oxygen inlet mole fraction [-]	0.153
Cell temperature [K]	343.15
Absolute anode pressure [Pa]	$1 \cdot 10^5$
Absolute cathode pressure [Pa]	$1 \cdot 10^5$
Hydrogen stoichiometry	1.2
Oxygen stoichiometry	2.5

3.3. Numerical Setup

The two different PEMFC devices are simulated in the open-source finite volume CFD code OpenFOAM. A volumetric description of the CL, MPL, GDL and MEM is applied in

this work. Moreover, the ions and electrons transfer inside the bipolar plates and the MEM is 3D modeled. A steady-state approach is considered for the numerical assessment of the two PEMFC configurations. The adopted convergence criterion is based on the computed current densities. In order to discretize the Navier–Stokes equations in the fluid region, second-order numerical schemes are adopted. In particular for the divergence term, a limited linear numerical scheme is adopted for density and velocity computation, while a Van Leer numerical scheme is used for the multi-phase assessment. The computational grids for the discretization of the different domains have been selected with a grid sensitivity analysis conducted during the study and they are hereafter described.

3.3.1. Parallel Flow Channel Computational Domain

The parallel flow channel configuration consists of 24 cathodic and 25 anodic channels, as described in Section 3.1. To reduce the computational cost of the numerical simulations, the periodicity of the flow-field structure is exploited. Indeed, it is reasonable to assume that adjacent channels share homogeneous conditions, since a manifold is placed at both the inlet and outlet of the channels. So, homogeneous gas distributions are obtained on the anode and cathode sides. Thus, half of a single anodic and cathodic channel only are considered for the CFD modeling. Additionally, the zero-gradient cell hardware is designed to achieve nearly homogeneous conditions along the longitudinal direction of the channels. Therefore, although the actual length of the active porous media is 50 mm, only 10 mm is modeled in the CFD framework to further reduce computational cost. This approach results in a simulated active surface area of 0.0425 cm^2 in the CFD model instead of 10 cm^2.

Two channel extrusions, at the inlet and outlet sides, are considered to assure the flow development before the fluid reaches the active area of the component. The discretization of the computational domain is computed using a regular hexahedral mesh, oriented with the flow-field geometry. The grid counts $4.6 \cdot 10^5$ hexahedral cells. In order to better discretize the complex phenomena occurring in the porous media, such as phase change or diffusion, a grading in the computational domain is used in the porous media and near the membrane, along the channel length. In Figure 4, the obtained computational domain is shown.
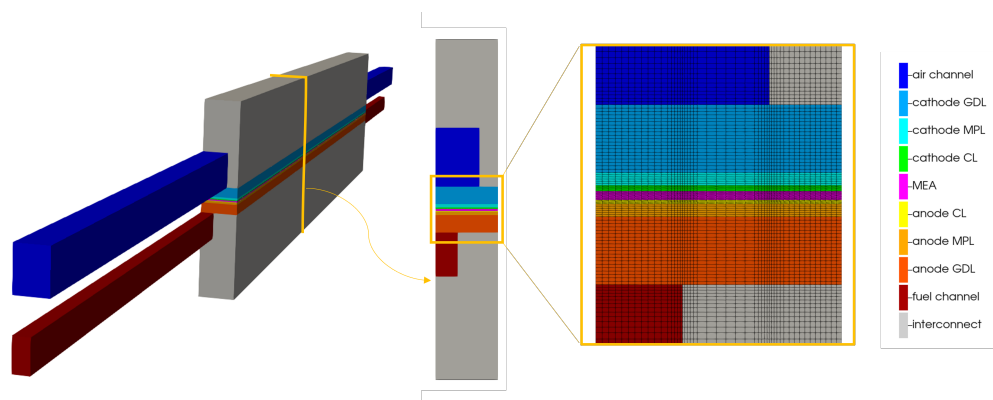
Figure 4. Computational domain of the parallel flow channel configuration.

3.3.2. Serpentine Flow Channel Computational Domain

Differently from the parallel flow channel configuration, for the serpentine one no periodicity or symmetry of the flow field can be exploited to reduce the computational domain. In fact, for this type of flow distributor, the convective flow created in the GDL and the interaction among adjacent channels must be taken into account in order to properly predict the component performance. The discretization of the computational domain is computed using a regular mesh oriented with the flow-field geometry. The grid counts 4.1×10^6 cells, most of them hexahedral while some polyhedral cells are present in the region where the flow-field channels and the GDL are put in contact. In Figure 5, the obtained computational domain is shown.
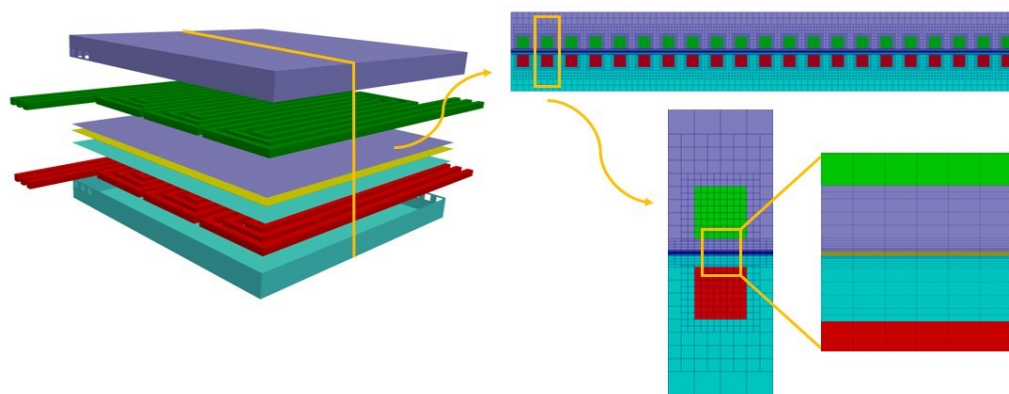
Figure 5. Computational domain of the serpentine flow channel configuration.

3.4. Model Setup

The validation of both the PEMFC configurations is carried out in terms of polarization curves, by imposing in the simulations the voltage across the bipolar plates and by comparing the predicted current densities with those experimentally measured at the test bench. The ionic conductivity is computed for the two components considering a volume fraction of Nafion equal to 0.3 in Equation (13). θ_{PtOx}, used to properly account for PEMFC operation at high voltages, is computed imposing the PtOx equilibrium potential equal to 0.83 V in Equation (21), with anodic and cathodic transfer coefficients equal to 0.25 in Equation (22). Regarding the electrochemical reaction rates (Equations (23) and (24)), an exchange current density of 2×10^9 A/m^3 is used for anodic reaction for both the configurations. Regarding the cathodic electrochemical reaction instead, exchange current densities of 5×10^6 A/m^3 and 1×10^6 A/m^3 are used for the parallel and the serpentine channel geometries, respectively. The anodic and cathodic transfer coefficients α^{an} and α^{cat} are made to be equal to 0.5 for both the configurations. The Nernst potential in Equation (27) is computed using an E_0 value of 0 V and 1.23 V for the anodic and cathodic side, respectively. Finally, the hypothesis of the laminar regime for the two configurations has been successfully verified on both the anode and cathode sides of the two configurations. Indeed, a maximum Reynolds number of 80 and 1000 is computed for the parallel and serpentine channel configuration, respectively, both observed on the cathode side.

4. Results

In this section, the two fuel cells previously described are simulated. The validation of the implemented methodology is carried out by comparing the results with experimental data in terms of the polarization curve. Then, a detailed analysis of the flow field is carried out to highlight how the distribution of the relevant quantities (reactant concentrations, current, temperature and platinum oxidation) are influenced by the geometry of the channel layouts.
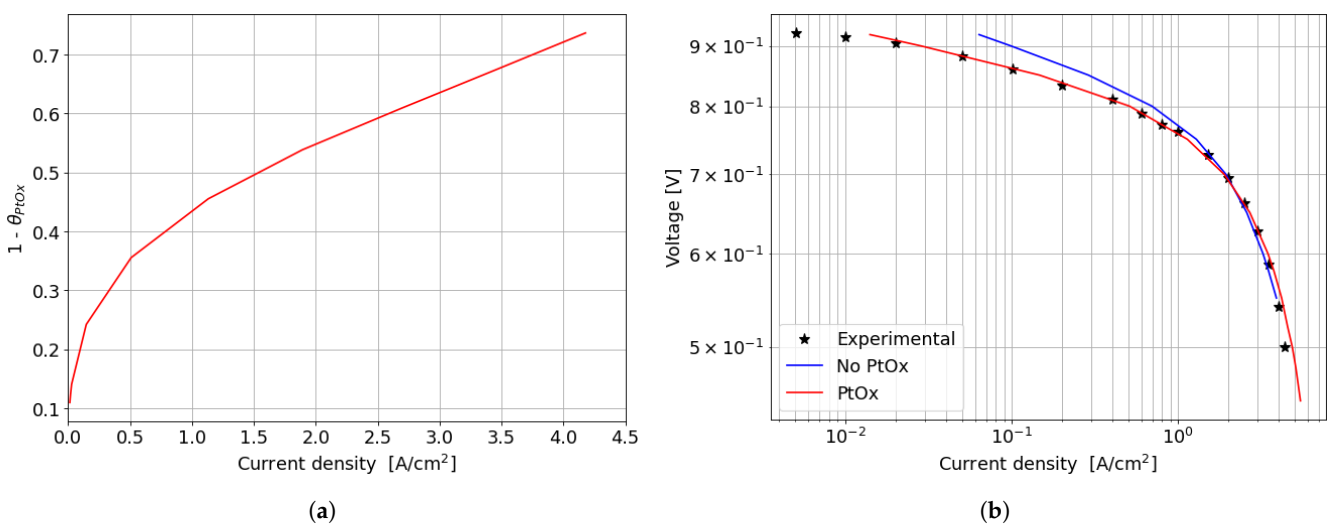
4.1. Parallel Channel Geometry

The comparison between the computed and measured polarization curves is shown in Figure 6; the power produced by the cell is also reported.

In the kinetic and ohmic regions, the numerically computed results closely match the experimental data. However, in the mass transfer region, numerical simulations tend to slightly overestimate cell performance in terms of current density produced, with a maximum percentage error of around 11% at 0.5 V. A consistent description of the ORR activation region at low current densities is provided by the adopted numerical methodology. In particular, in this region of the polarization curve, the PtOx formation process has a strong impact on the decrease in the fuel cell performance in terms of current density. In fact, the ORR kinetics is inhibited due to the coverage of the electrocatalyst surface by oxides that reduces the available surface for the electrochemical reaction. The cathode per-

formance may decrease up to 80% at low current densities, as shown in Figure 7a where the $(1 - \theta_{PtOx})$ factor is plotted. This is accounted for in the Tafel equation on the cathode side and it takes into account the ORR electrochemical reaction rate reduction. So, neglecting the formation of platinum oxides would lead to an overestimation of the fuel cell performance, which is particularly significant at low current density, as depicted in Figure 7b. At medium and high current densities instead the results obtained for the two different configurations are almost comparable since the oxidation of the Pt nanoparticle surface is minor and plays a negligible role in the high current region of the polarization curve.
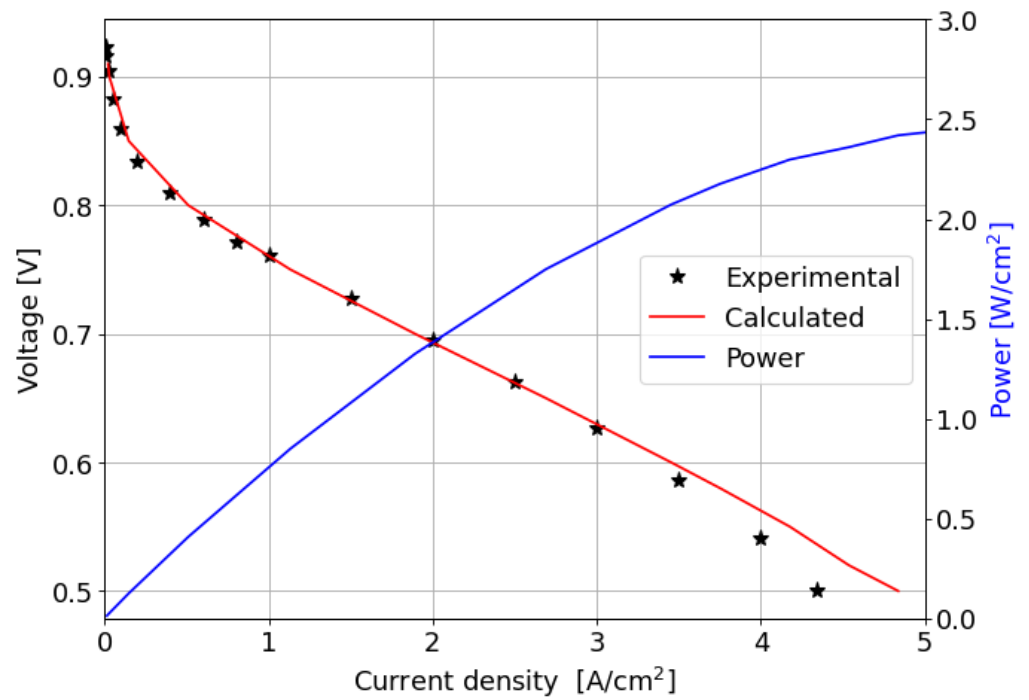
Figure 6. Experimental and numerically computed polarization curves and power produced for the parallel channel geometry.

Figure 7. Effect of PtOx formation on fuel cell performance for the parallel channel geometry. (**a**) PtOx coverage ratio as function of the current density for the parallel channel geometry. (**b**) Polarization curve in logarithmic scale when accounting or not for PtOx formation.

The voltage across the cell is linearly correlated to the current density in the ohmic region. Here, ohmic losses cause a linear voltage drop that originates from ion transfer through the porous media. In this portion of the polarization curve, the PEM fuel cell performance is accurately described by the applied methodology. As previously described, a correction coefficient $\xi = 3$ is used in the ionic conductivity model (Equation (13)) to improve the match between the computational results and experimental data. Other ohmic phenomena may be the origin for this correction factor, e.g., an underestimation of the electrical conductivity of the porous materials or the isotropic assumption for the same. Instead, the conductivity properties of these materials, for example the GDL, are more realistically orthotropic since preferential conductivity paths in the in-plane direction are detected, due to the carbon fiber orientation. This feature may justify the requirement for a correction coefficient on ionic conductivity. In future works, this aspect will be investigated more in details.

In the mass transfer region, the numerical results slightly overestimate the experimental data. At a high current density, the water produced by the electrochemical reactions increases and it may partially condensate. Liquid water in the porous media may cause a partial pore block effect, thus reducing the reactant diffusion toward the active area on the cathode side. For this reason, a correct modeling of the condensed water is fundamental for a correct prediction of the fuel cell performance. An underestimation of the water content in the porous media may be a reason for the overestimation of the experimental data in this region.

In order to better understand the parallel flow channel working operation, some of the most significant physical quantities distribution are now depicted and analyzed. In particular, the operating point at V = 0.7 V is considered. This working condition is taken into account since it is representative of the ohmic region operating condition, where the fuel cell would work for the majority of its service life. In Figure 8, the oxygen, hydrogen and water vapor concentrations evaluated at the middle channel cross-section are shown. Moreover, since a multi-phase flow on the cathode side is modeled, the volumetric liquid water fraction for the cathode side is reported too. Finally, since the parallel flow channel configuration is zero-gradient cell hardware, only through-plane reactant concentrations are shown, where the major gradients can be detected. The molar concentration of oxygen and hydrogen is higher in the channel and lower under the rib, as expected, due to the diffusion losses occurring in the porous media. At the same time, the water vapor molar concentration and the volume liquid water fraction are higher under the rib with respect to the channel. Water is produced by the electrochemical reactions on the active surface area. As the diffusion of the reactants towards the active sites is less favored under the rib, at the same time the diffusion of water from the active sites towards the channel is unfavored as well. So, due to the diffusion losses inside the porous media, both water and vapor tend to accumulate under the rib, partially blocking the pores.

The reactant distribution directly affects the current density in-plane distribution produced in the membrane. In Figure 9, some relevant quantities computed on the membrane middle cross-section are illustrated: current density, temperature, water content λ and oxide coverage of the electrocatalyst. Coherently with the liquid water fraction distribution shown in Figure 8, λ is higher under the rib compared to the region under the channel. In fact, due to the diffusion losses occurring in the porous media, the vapor and the condensed liquid water produced tend to accumulate under the rib. Hence, a higher electrical conductivity is detected under the rib, so the current density produced shows a peak in this region and a lower computed value under the channel. Concerning the temperature field on the membrane in-plane section instead, it shows a higher value under the channel than under the rib. This is due to the fact that the bipolar plate shows a higher thermal conductivity compared to the channel, thus ensuring better heat removal under the rib leading to a lower temperature in this zone. Moreover, it is interesting to evaluate the oxide coverage of platinum: due to the low current density, corresponding to a high overpotential, the coverage is quite high, around 0.88. On the other hand, the

oxidation is quite uniform, resulting in a homogeneous reduction in the performance of the fuel cell in both the channel and rib zone.
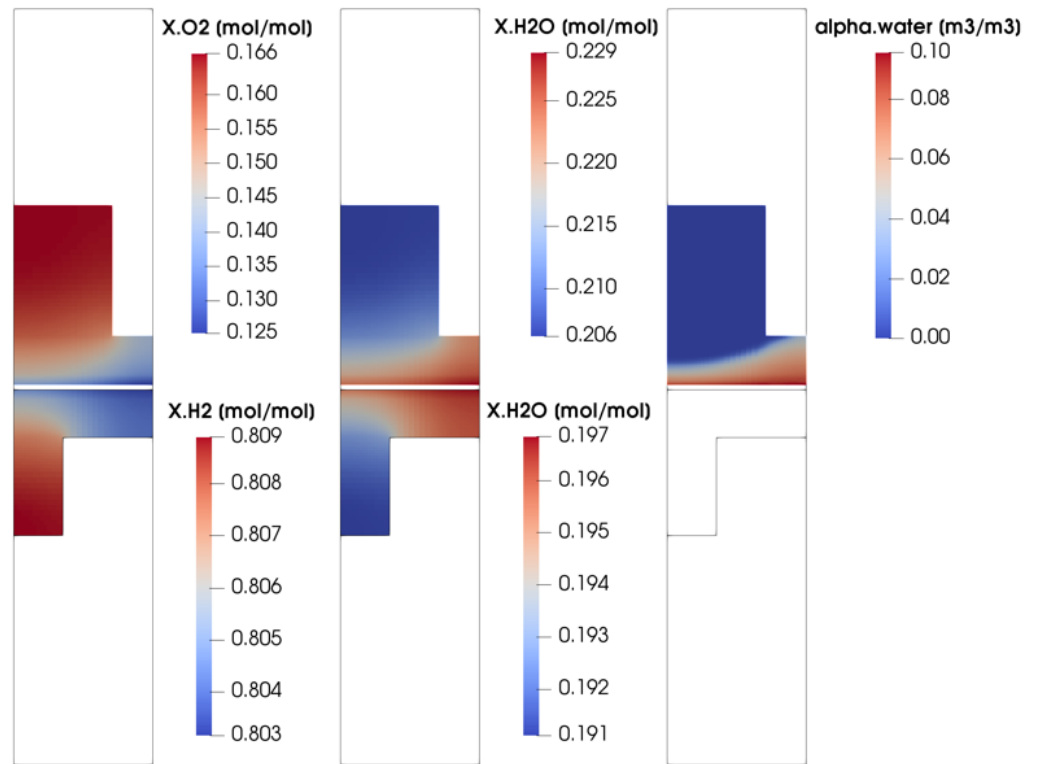
Figure 8. Reactant molar concentration and water saturation evaluated at the middle channel cross-section for V = 0.7 V.
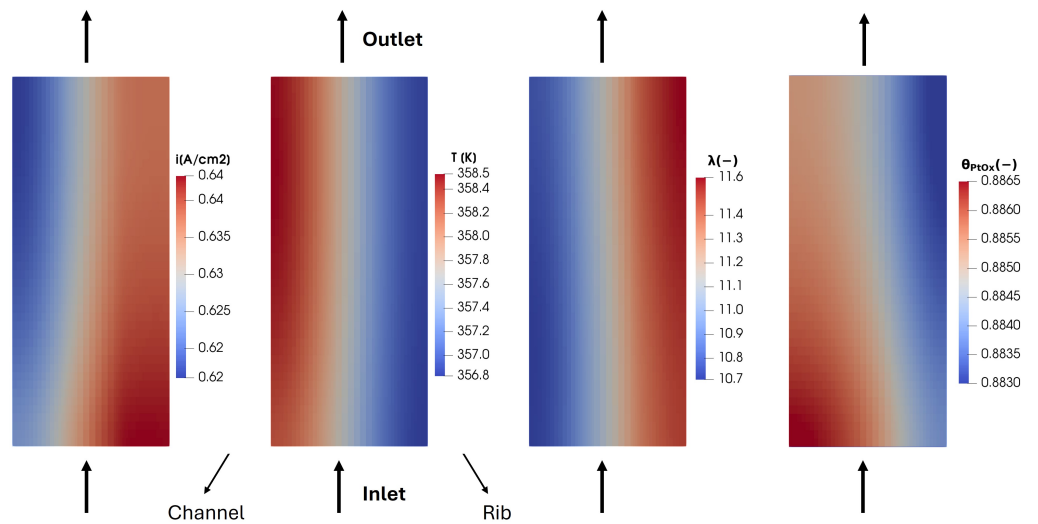
Figure 9. Membrane in-plane current density, temperature and λ together with oxide coverage of the electrocatalyst computed in the CCL for V = 0.7 V.
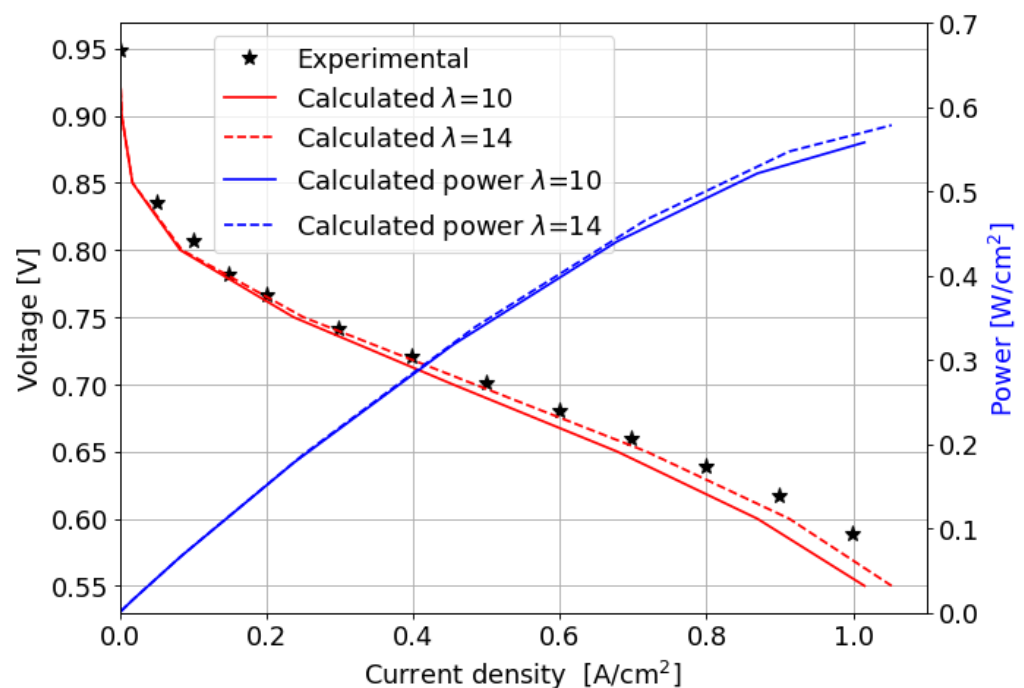
4.2. Serpentine Channel Geometry

The validation procedure for the serpentine channel geometry is carried out considering a single-phase flow. So, the condensation of water is not accounted for on the cathode side of the component since the analysis is focused on a low current density range only up to 1 A/cm². In this condition, the water produced by electrochemical reactions is low. Hence, water accumulation in the channel and pore blockage effects are negligible. On the other hand, the presence of only vapor has the effect of promoting the humidification of

the membrane. For this reason, MEA is modeled as an impermeable solid medium and the water content λ is assumed as uniform, considering two different cases with λ equal to 10 and 14.

Similarly to the analysis performed on the parallel channel configuration, a comparison between the numerically computed and experimentally measured polarization curves is shown in Figure 10, together with the calculated cell power. The two polarization curves are computed with a water content equal to 10 and 14, respectively, while the power is reported for the second case only. As expected, the reduction in the water content leads to a lower performance, since the membrane ionic conductivity linearly depends on λ. However, the impact is pretty negligible in the kinetic region and is quite limited in the ohmic region where the present analysis is focused, as demonstrated by the comparison between the two cases. A good agreement between the experimental data and numerically computed performance is found when $\lambda = 14$ is considered. Thus, this condition will be considered for the following analysis.

Figure 10. Experimental and numerically computed polarization curves and computed power produced for the serpentine channel geometry.

The applied methodology gives a consistent description of the fuel cell performance either in the ORR activation or in the ohmic regions of the polarization curve. At high voltages, the cell performance is influenced by the formation of PtOx, which cover the active sites thus decreasing the catalytic activity. In particular, the factor $(1-\theta_{PtOx})$, describing the impact of PtOx formation, reduces the ORR electrochemical reaction rate by 60% and 80% at high voltages/low current densities, compared to an ideal electrochemical kinetic where this mechanism is not taken into account (Figure 11a). Moreover, it must be pointed out that the outcomes in terms of performance reduction are similar to those found for the parallel channel geometry. In Figure 11b, two different polarization curves are plotted in a logarithmic scale and compared with the experimental data. The curve labeled as *PtOx* is the same polarization curve obtained making $\lambda = 14$ as shown in Figure 10. On the other hand, the curve labeled as *No PtOx* is obtained with the same set up as the *PtOx* curve but the PtOx formation mechanism is not accounted for. Similarly to what is obtained for the parallel channel geometry in Figure 7a, if the PtOx formation kinetic is neglected, an overestimation of the fuel cell performance at high voltages is computed.

(**a**)

(**b**)
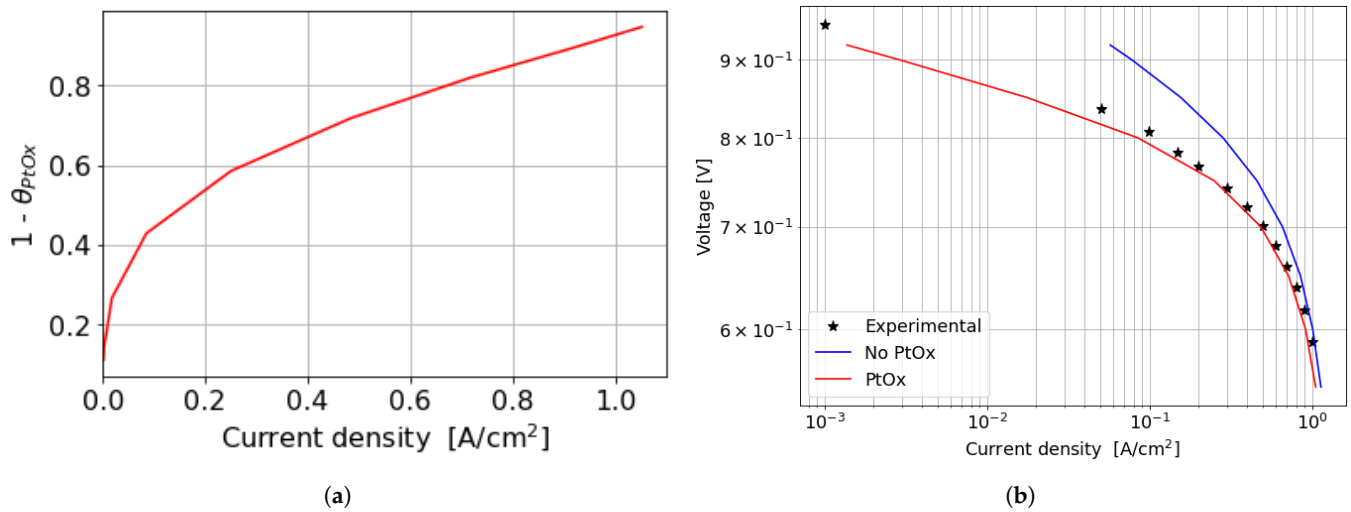
Figure 11. Effect of PtOx formation on fuel cell performance for the serpentine channel geometry. (**a**) PtOx coverage ratio as function of the current density for the serpentine channel geometry. (**b**) Polarization curve in logarithmic scale when accounting or not for PtOx formation.

In order to better understand the operation of the serpentine configuration, different physical quantities together with their distribution over the channel flow field are analyzed in detail. In particular, the simulated operating condition at V = 0.7 V is considered since it is representative of the ohmic region operating condition where the fuel cell would work for the majority of its service life.

In Figure 12, the pressure field is shown. It is evaluated on a cross-section located at half of the channel height on the cathode and anode sides on the left and right, respectively. While the outlet pressure is fixed and set equal to the ambient pressure for both the flow fields, the inlet pressure is maximum for the cathode side, resulting in a higher pressure drop with respect to the anode side. The velocity field for the same cross-section for both the anodic and cathodic flow fields is shown in Figure 13. Even if the flow velocity is higher on the cathode side due to the higher stoichiometric factor, the velocity trends are similar for the two flow fields as expected. In particular, the highest velocity values are detected in the straight part of the flow field, while the flow is slowed down corresponding with the right-angle bends. As expected, in this part of the distributor, the flow velocity is almost null at the corners and a flow-field remixing process can be detected after the bend.
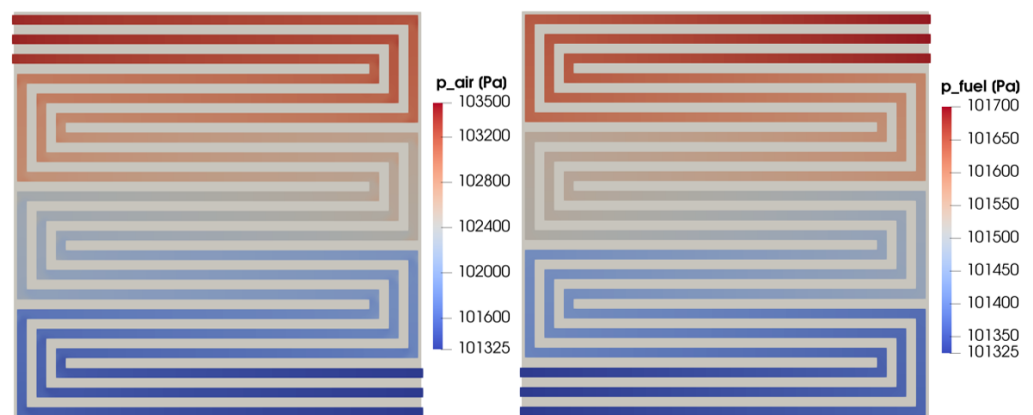

Figure 12. Cathode and anode pressure field at half height of the channel for V = 0.7 V.
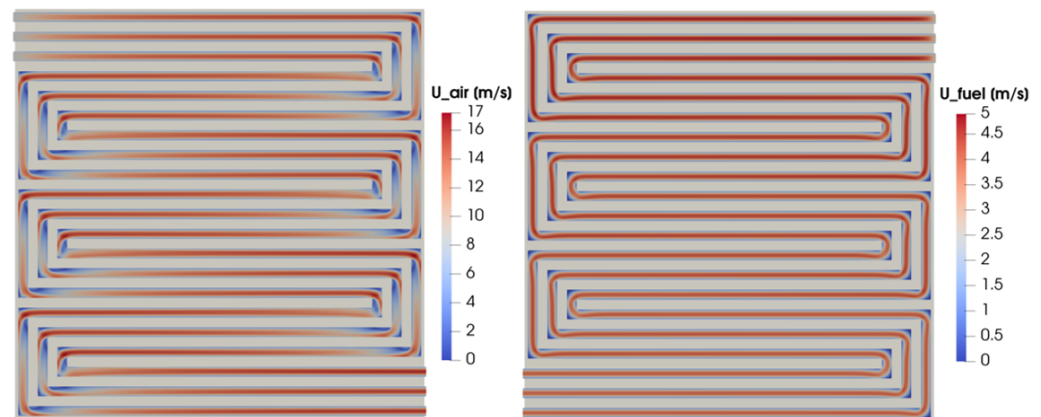
Figure 13. Cathode and anode channel velocity field at half height of the channel for V = 0.7 V.

The reactant concentration over the anode and cathode flow fields are shown in Figure 14 on the right and left side, respectively. Concerning the hydrogen concentration (shown on the right), it decreases from the inlet to the outlet in the channels since it is consumed by the electrochemical reactions. Looking at the hydrogen concentration under the rib instead, it must be pointed out that it is lower with respect to the one in the neighboring channel due to the lower diffusivity of the porous media. Moreover, the hydrogen concentration under the rib decreases from the inlet to the outlet coherently with the hydrogen concentration in the channels. Concerning the oxygen concentration, it decreases from the inlet to the outlet in the channels since it is consumed by the electrochemical reactions, similarly to what happens for hydrogen on the anode side. However, the difference between the oxygen concentration under the rib and in the neighboring channel is higher with respect to what is detected for hydrogen on the anode side. This is due to the lower oxygen diffusivity in the porous media compared to the hydrogen one. Finally, the oxygen concentration under the rib decreases from the inlet to the outlet coherently with the oxygen concentration in the channels and with the hydrogen distribution at the anode.
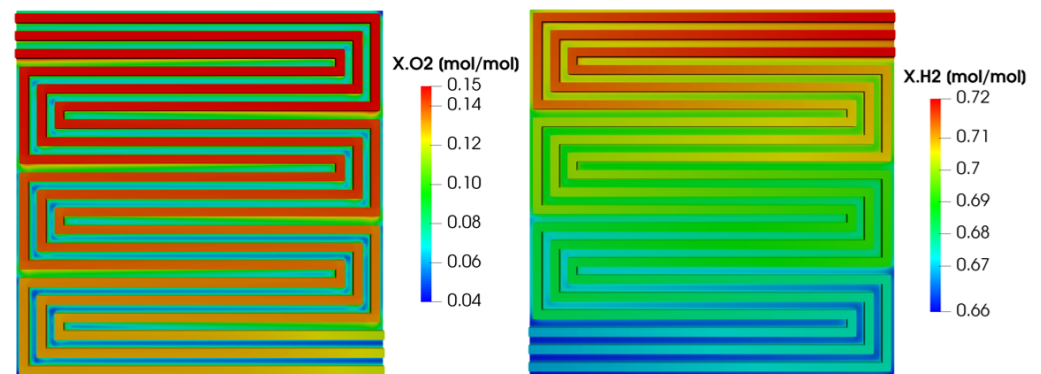
Figure 14. Reactant concentration in the anodic and cathodic channels for V = 0.7 V.

The reactant distribution over the active surface is the result of the flow in the channels, driven by the convection, and the transport of the species in the porous layers, driven by the diffusion. However, the difference in pressure exiting between adjacent channels enhances the reactant diffusive transport in the GDL, establishing a convection contribution. The cross-flow from channel to channel through the GDL is visualized in Figure 15, which refers to a cross-section located at the mid-height of the GDL, illustrating the in-plane velocity field on both the cathode and anode sides. It can be seen that the in-plane velocity magnitude is higher for the cathode side, corresponding to the higher channel velocity and pressure gradient along the channels compared to the anodic side. However, the computed in-plane velocity trends are the same for both sides, as expected. In particular, a velocity peak is detected where the pressure gradient between two adjacent channels is the

highest (indicated as points A, B, C, D, E and F). For example, at point B, the conformation of the serpentine configuration leads to a significant pressure gradient between the two adjacent channels, higher than elsewhere, resulting in a peak of the cross-flow through the porous layer.
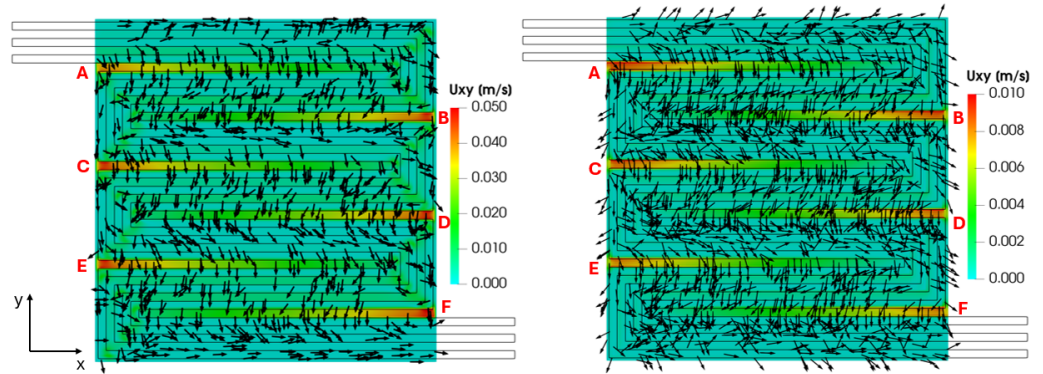

Figure 15. GDL in-plane velocity field on the cathode (**left**) and anode side (**right**) sides for V = 0.7 V.

To further examine the effect of convective flows originating in the GDL between different channels, a transversal cross-section relative to the flow field is considered in Figure 16, highlighting the velocity field in the *yz* plane. As expected, the velocity magnitude is higher on the cathode side compared to the anode side, consistent with the observations in Figure 13. Additionally, on the anode side, a velocity peak is detected in the porous media every three channels, corresponding to the pressure gradient peaks between channels, as shown in Figure 15. On the cathode side, however, the velocity profiles differ from the anode side, resulting in a vortex flow field after the first three channels, following the first bend of the flow field. These flow patterns are illustrated using glyphs, as shown for the first and last channel cross-sections. Specifically, at the inlet, the flow field does not exhibit any distinct pattern, while, starting from the second channel cross-section triplet, a vortex structure can be observed on the cathode side. Within the porous media, the flow field aligns with the pressure field, flowing from the inlet to the outlet.
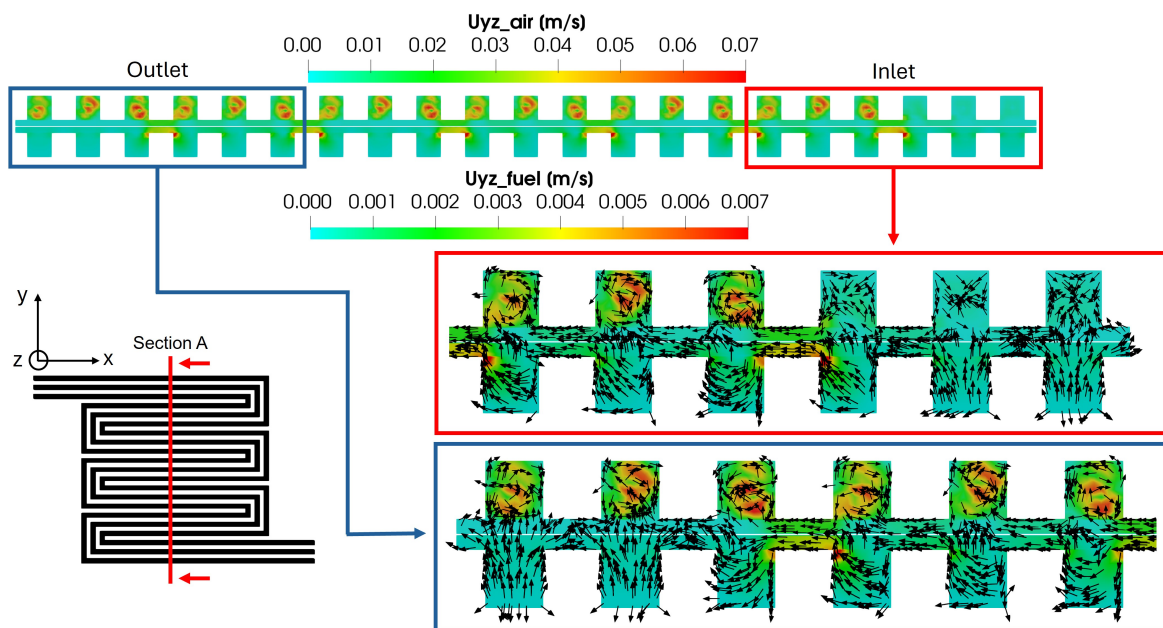

Figure 16. Convective flow in anode and cathode flow field.

The convective flow that arises in the GDL directly affects gas distribution in the channels and porous media. Figure 17 shows the reactant concentrations in *Section A* for both the anode and cathode sides. As expected, and in line with the reactant distribution seen in Figure 14, both oxygen and hydrogen concentrations decrease from the inlet to the outlet due to their consumption in the electrochemical reactions. Focusing on the through-plane reactant distribution, concentrations are lower under the rib compared to under the channel, due to the diffusivity of oxygen and hydrogen in the porous media. However, the concentration gradient between the channel and the porous media under the rib is lower on the anode side than on the cathode side. This is because the diffusivity of oxygen in the porous media is lower than that of hydrogen, resulting in a less homogeneous distribution. Moreover, the oxygen concentration gradient tends to be symmetrical with respect to the channel cross-section, though some exceptions occur. In particular, every three channels, an asymmetry in the oxygen distribution is detected in the direction of the convective flow. The pressure gradient that arises before and after the bend of the same channel causes a convective flow in the porous media, as shown in Figure 16. This results in increased reactant diffusion and consequently higher concentrations under the rib.
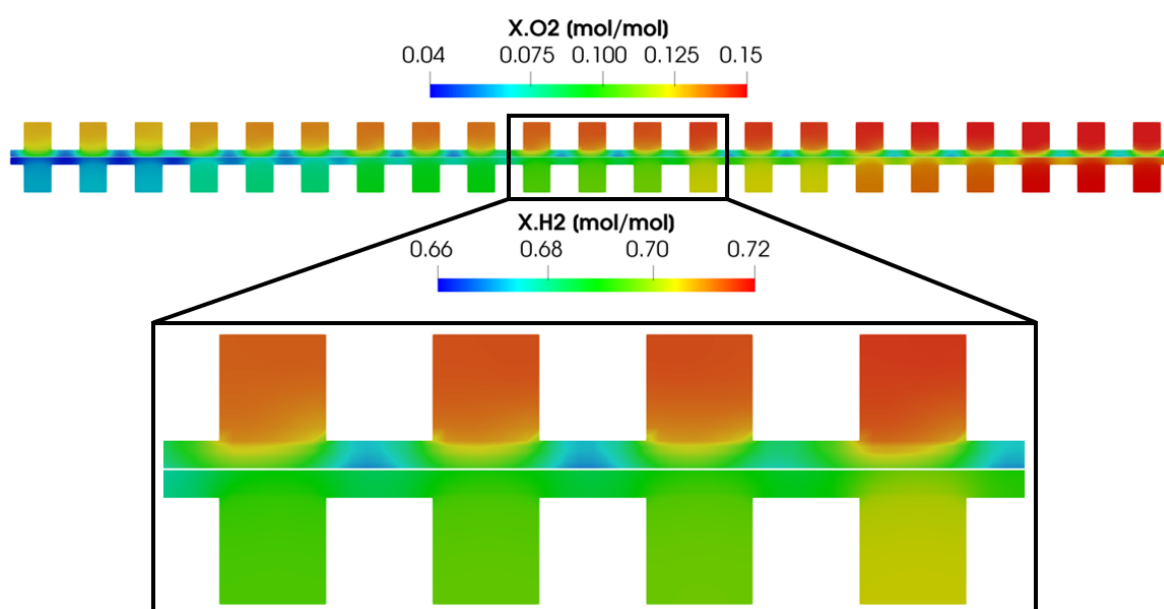

Figure 17. Reactant distribution in the anodic and cathodic channel cross-section (section A).

In Figure 18, different physical quantities calculated in Section B are shown. This cross-section considers the same channel at a distance of nearly twice the cell side length. So, for the sake of simplicity, the two different channel sections are called upstream and downstream. This particular section has been chosen to highlight the effects of the pressure gradient among the upstream and downstream channels on the convective flow and reactant distribution in the porous media. The pressure gradient between the upstream and downstream channels is significantly higher on the cathode side, around 500 Pa, compared to approximately 100 Pa on the anode side. This pressure gradient induces a convective flow in the porous media from the upstream to the downstream channel, as indicated by the glyphs in the figure. Consequently, it causes an uneven oxygen distribution under the upstream channel on the cathode side, resulting in an increased oxygen concentration under the rib between the upstream and downstream channels. Additionally, the channel velocity profile in Figure 18 shows that the upstream channel exhibits a disturbed flow field on the cathode side due to the bend in the duct, consistent with the findings in [51]. This disturbance is not detected in the downstream channel since the analyzed cross-section is placed before the subsequent duct bend.
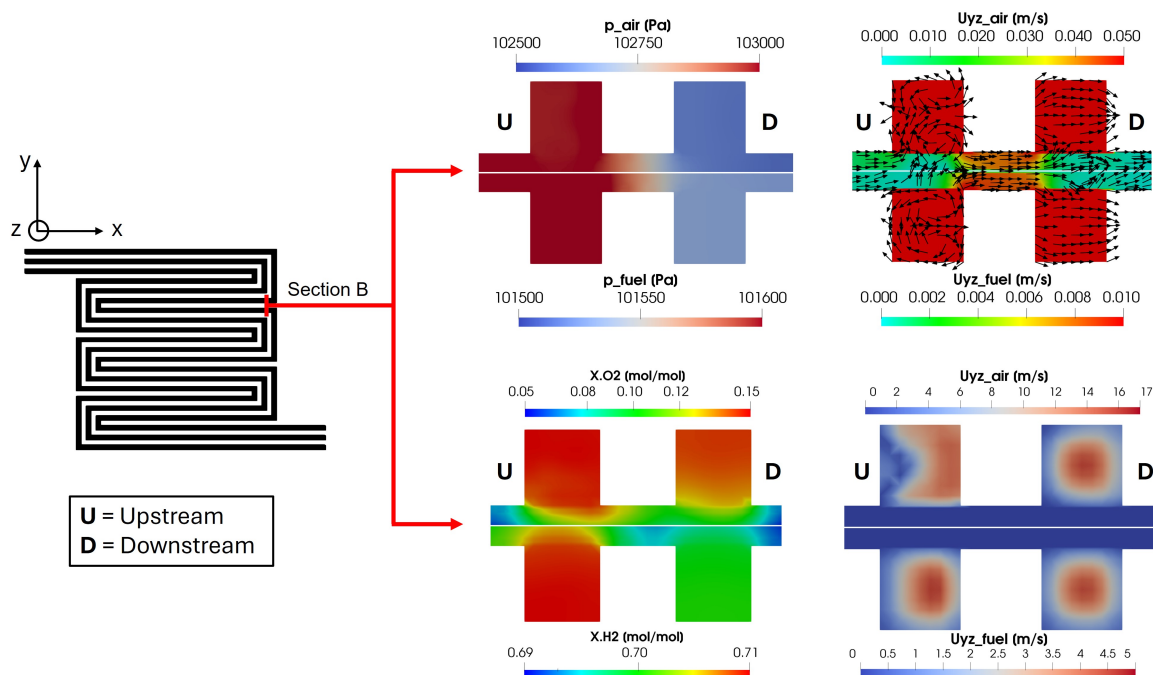
Figure 18. Pressure convective flow and reactant distribution in Section B for upstream and downstream channels. The yz velocity field is shown twice with two different scales in order to focus separately on porous media and channels.

The calculated in-plane velocity profile in the GDL and in the porous media, along with the reactant distribution shown in Figures 15–18, affects the distribution of the produced current density. In Figure 19, the membrane in-plane produced current is shown. As expected, the computed current density is higher under the channel compared to under the rib. This is consistent with the reactant concentration distribution (Figure 14) which is higher under the channel due to the diffusivity losses in the porous media under the rib. Moreover, some peaks are detected in the calculated current density. In particular, they are located where a pressure gradient is detected between two adjacent channels, as in Section B between the upstream and downstream channels, causing a convective flux through the GDL. This occurs at points A, B, C, D, E and F in Figure 15. In these portions of the membrane, the current density computed under the rib is comparable with the one produced under the channel. Thus, the convective flow in the GDL and the resulting higher reactant concentration lead to improved local fuel cell performance.
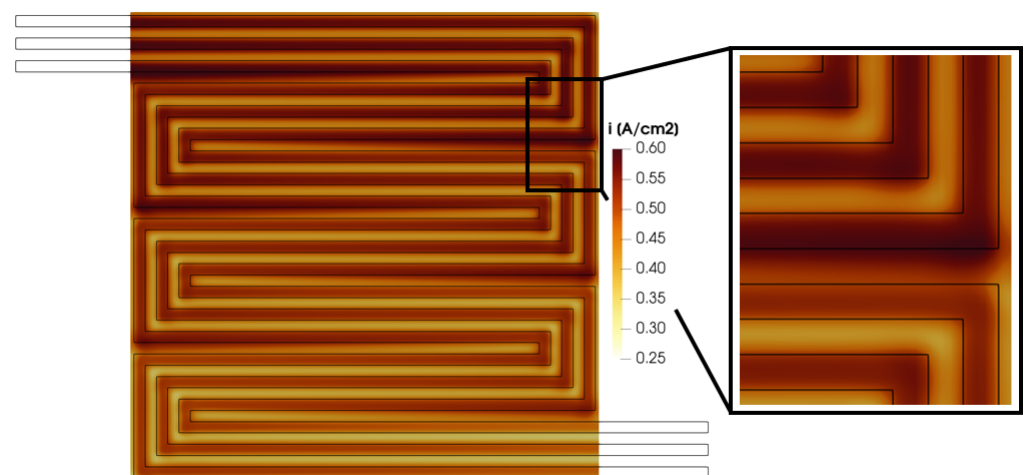
Figure 19. Membrane in-plane current density for V = 0.7 V.

The local increase in performance shown in Figure 19 indicates a rise in the electrochemical reaction rate, which is an exothermic process and might typically lead to an undesired local hot spot in this portion of the membrane. However, the temperature under the rib is lower than under the channel in this specific area, as highlighted in Figure 20. This difference between the membrane in-plane current density trend and the temperature trend is due to the high thermal conductivity of the bipolar plate, which ensures effective heat removal. Consequently, the temperature under the rib is lower than under the channel. These trends in current density and temperature across the membrane are advantageous. They suggest that creating a convective flow in the porous media can enhance local performance without forming unwanted hot spots that could accelerate fuel cell degradation.
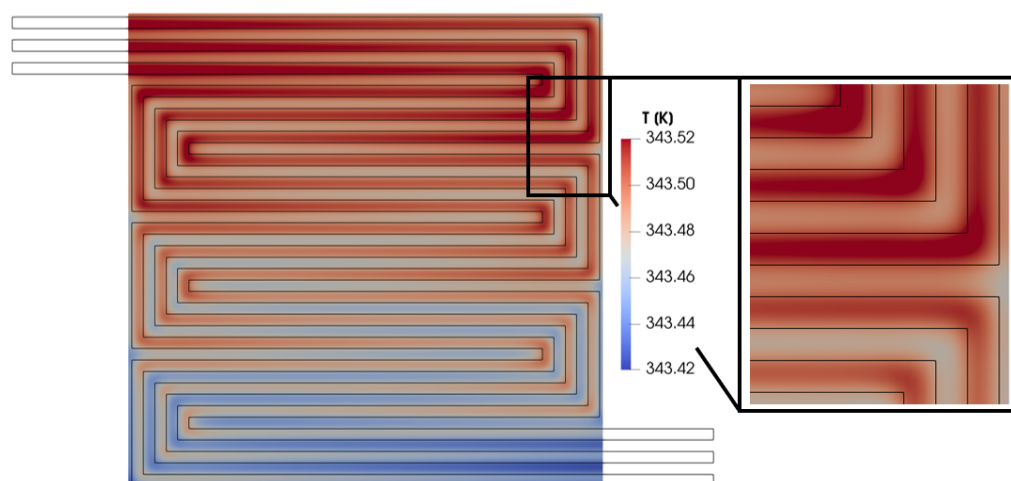

Figure 20. Membrane in-plane temperature distribution for V = 0.7 V.

Finally, the oxidation status of the platinum catalyst is analyzed in Figure 21. Although the average PtOx value is relatively low, it exhibits significant variability across the plane. In particular, the maximum value is reached under the channel and in regions with high catalytic activity, which are characterized by intense current densities but also by high electric potential, which is directly responsible for the PtOx formation.
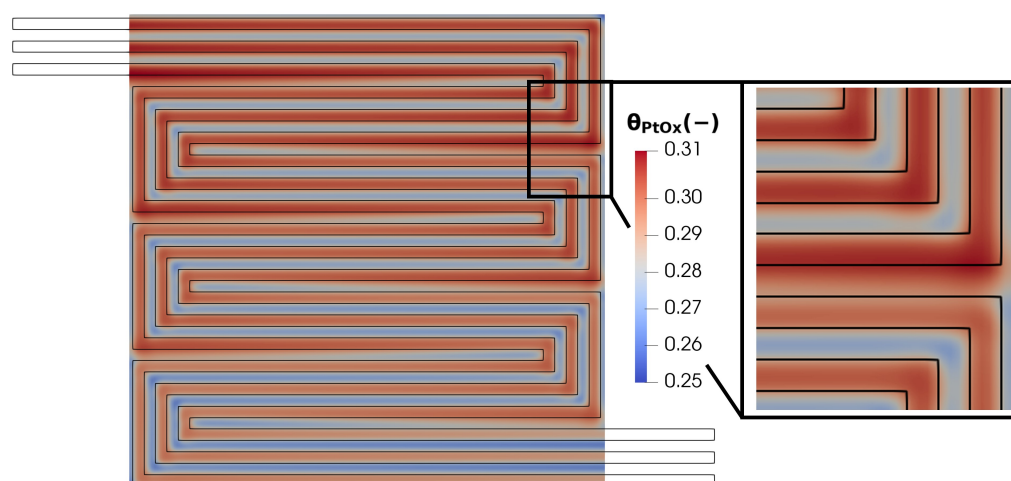

Figure 21. Membrane in-plane θ_{PtOx} factor distribution for V = 0.7 V.

5. Conclusions

In this work, the performance of two different fuel cell configurations—a parallel flow channel configuration and a serpentine flow-field geometry—have been numerically investigated. An open-source CFD simulation library has been applied for the analysis. A

multi-phase flow on the cathode side is considered for the parallel flow channel configuration. On the other hand, a single-phase approach with an imposed λ value has been considered for the serpentine geometry since only low current density region is investigated. For both the configurations, the applied methodology has been validated against experimental data. Then, the distribution of the most significant physical quantity fields are analyzed in detail. The main outcomes of the paper are now presented.

1. From the comparison between the experimental data and numerical results, it is evident that the PtOx kinetic mechanism must be considered not to overestimate fuel cell performance. In particular, the most critical condition in terms of inhibition of the oxygen reduction reaction on the cathode side is observed at high voltages. In fact, in this part of the polarization curve, the reduction in performance due to this mechanism is the highest, reaching up to 60–80% performance reduction for the two analyzed configurations.
2. The adopted methodology provides an accurate description of PEM fuel cell operating conditions for different flow-field configurations. The investigation of the main operation characteristics in the kinetic and ohmic regions is carried out for both parallel and serpentine channel geometries. The effect of the distributor geometry on the reactant diffusivity and distributions is highlighted and it is put in correlation with the component performance.
3. A detailed analysis of the most significant in-plane and through-plane physical quantity distributions such as pressure, velocity and reactant concentration for the serpentine channel geometry allowed highlighting some local performance peaks. In particular, the produced current density peaks originate where a local increase in convective flow arises in the GDL due to a local increase in the pressure gradient. Moreover, the local increase in performance can be coupled with the absence of undesired local hot spots in the active surface area. This is due to the higher thermal conductivity of the bipolar plate with respect to that of the fluid flowing into the channel. So, it allows the fuel cell performance to grow avoiding degradation.
4. The porous media anisotropy should be accounted for in future improvements of the adopted numerical model. In particular, the effect of the presence of preferential directions for both thermal and electrical conduction on the fuel cell performance should be taken into consideration. Moreover, further improvements to the numerical model should be focused on the estimation of the ionic conductivity in the MEA, which plays an important role in the predictivity in the ohmic region, and of the water formation/accumulation, relevant at a medium/high current.

Author Contributions: Conceptualization: M.B. and A.D.T.; Methodology: M.B., A.D.T., A.B. and A.G.; Software: M.B., A.D.T. and G.M.; Results analysis: M.B., A.D.T., A.B., A.G., L.M. and R.M.; Writing: M.B. and A.D.T.; Review: M.B., A.D.T., A.B., A.G., L.M., R.M., G.M. and A.O.; Supervision: A.D.T., R.M. and A.O.; Funding: A.B. All authors have read and agreed to the published version of the manuscript.

Data Availability Statement: The raw data supporting the conclusions of this article will be made available by the corresponding author on request.

Conflicts of Interest: The authors declare that they have no known competing financial interests or personal relationships that could have appeared to influence the work reported in this paper.

Abbreviations

The following abbreviations are used in this manuscript:

3D	Three Dimensional
ACL	Anodic Catalyst Layer

CFD	Computational Fluid Dynamics
CL	Catalyst Layer
CCL	Cathodic Catalyst Layer
ECSA	Electrochemically Active Surface Area
EOD	Electro-osmotic Drag
EW	Equivalent Weight
GDL	Gas Diffusion Layer
HOR	Hydrogen Oxidation Reaction
MEA	Membrane Electrode Assembly
MEM	Membrane
MPL	Micro Porous Layer
ORR	Oxygen Reduction Reaction
PEM	Polymer Electrolyte Membrane
PEMFC	Polymer Electrolyte Membrane Fuel Cell
PTFE	Polytetrafluoroethylene
RHE	Reversible Hydrogen Electrode
a	Water activity [-]
C	Concentration [-]
c_P	Specific heat at constant pressure [J/kgK]
D	Diffusion coefficient [m^2/s]
E_{Nernst}	Nernst potential [V]
EW	Equivalent weight [mol/m^3]
F	Faraday's constant [C/mol]
g	Acceleration due to gravity [m/s^2]
J	Electric transfer source/sink [A/m^3]
j	Electrochemical reaction rate [A/m^3]
h	Enthalpy [J/kg]
i	Current density [A/m^3]
K	Permeability [m^2]
K_r	Relative permeability [-]
k	Thermal conductivity [W/mK]
M	Interphase momentum transfer [kg/m^{2}s^2]
M	Molar mass [kg/kmol]
m	Rate of mass transfer [mol/s]
n_d	Electro-osmotic drag coefficient [-]
p	Pressure [Pa]
S_{Darcy}	Darcy's term [kg/m^{2}s^2]
R	Mass source/sink [kg/m^{3}s]
R	Universal gas constant [J/molK]
T	Temperature [K]
U	Equilibrium potential [V]
U	Mixture velocity [m/s]
x	Molar fraction [-]
Y	Mass fraction [-]
α	Phase saturation [-]
α	Transfer coefficient [-]
Γ	Thermal diffusivity [m^2/s]
ϵ	Porosity [-]
η	Activation overpotential [V]
λ	Water content [mol/m^3]
μ	Dynamic viscosity [kg/ms]
ω	Energy parameter for Temkin isotherm [kJ/mol]
ρ	Density [kg/m^3]
σ	Ionic conductivity [S/m]
σ	Surface tension [N/m]
θ	Contact angle [°]
θ_{PtOx}	PtOx coverage ratio [-]
Φ	Potential [V]
ϕ	Electric potential [V]

References

1. Liu, Z.; Cai, S.; Tu, Z.; Chan, S.H. Recent development in degradation mechanisms of proton exchange membrane fuel cells for vehicle applications: Problems, progress, and perspectives. *Energy Storage Sav.* **2024**, *3*, 106–152. [CrossRef]
2. Jiao, K.; Li, X. Water transport in polymer electrolyte membrane fuel cells. *Prog. Energy Combust. Sci.* **2011**, *37*, 221–291. [CrossRef]
3. Moydien, H.; Levecque, P.; Susac, D. Experimental study of water management and performance of titanium fibre felts as versatile gas diffusions layers for PEMFCs. *Int. J. Hydrogen Energy* **2023**, *48*, 32968–32981. [CrossRef]
4. Xu, H.; Bührer, M.; Marone, F.; Schmidt, T.J.; Büchi, F.N.; Eller, J. Effects of gas diffusion layer substrates on PEFC water management: Part I. Operando liquid water saturation and gas diffusion properties. *J. Electrochem. Soc.* **2021**, *168*, 074505. [CrossRef]
5. Chen, T.; Liu, S.; Zhang, J.; Tang, M. Study on the characteristics of GDL with different PTFE content and its effect on the performance of PEMFC. *Int. J. Heat Mass Transf.* **2019**, *128*, 1168–1174. [CrossRef]
6. Wang, X.; Qu, Z.; Ren, G. Collective enhancement in hydrophobicity and electrical conductivity of gas diffusion layer and the electrochemical performance of PEMFCs. *J. Power Sources* **2023**, *575*, 233077. [CrossRef]
7. Liu, H.; Hu, Z.; Li, J.; Xu, L.; Shao, Y.; Ouyang, M. Investigation on the optimal GDL thickness design for PEMFCs considering channel/rib geometry matching and operating conditions. *Energy* **2023**, *282*, 128780. [CrossRef]
8. Dong, G.; Huang, G.; Wu, Z.; Li, Z.; Ming, P.; Zhang, L. Experimental and numerical study on the two-phase flow inside a cracked gas diffusion layer of PEMFC. *Int. J. Hydrogen Energy* **2024**, *50*, 18–31. [CrossRef]
9. Xiao, L.; Bian, M.; Sun, Y.; Yuan, J.; Wen, X. Transport properties evaluation of pore-scale GDLs for PEMFC using orthogonal design method. *Appl. Energy* **2024**, *357*, 122445. [CrossRef]
10. Yin, B.; Xu, S.; Yang, S.; Dong, F. Influence of microelliptical groove gas diffusion layer (GDL) on transport behavior of proton exchange membrane fuel cell (PEMFC). *Int. J. Heat Mass Transf.* **2021**, *180*, 121793. [CrossRef]
11. Ye, L.; Qiu, D.; Peng, L.; Lai, X. Conduction mechanism analysis and modeling of different gas diffusion layers for PEMFC to improve their bulk conductivities via microstructure design. *Appl. Energy* **2024**, *362*, 122987. [CrossRef]
12. Yablecki, J.; Bazylak, A. Determining the effective thermal conductivity of compressed PEMFC GDLs through thermal resistance modelling. *J. Power Sources* **2012**, *217*, 470–478. [CrossRef]
13. Cheng, M.; Luo, L.; Feng, Y.; Feng, Q.; Yan, X.; Shen, S.; Guo, Y.; Zhang, J. Numerical studies on porous water transport plates applied in PEMFCs under pure oxygen condition. *Appl. Energy* **2024**, *362*, 122903. [CrossRef]
14. Manso, A.; Marzo, F.; Barranco, J.; Garikano, X.; Garmendia Mujika, M. Influence of geometric parameters of the flow fields on the performance of a PEM fuel cell. A review. *Int. J. Hydrogen Energy* **2012**, *37*, 15256–15287. [CrossRef]
15. Yan, H.; Zhang, W.; Qu, Z.; Chen, N. Flow field plate of polymer electrolyte membrane fuel cells: A review. *J. Renew. Sustain. Energy* **2023**, *15*, 012701. [CrossRef]
16. Corda, G.; Cucurachi, A.; Diana, M.; Fontanesi, S.; D'Adamo, A. A Methodology to Design the Flow Field of PEM Fuel Cells. *SAE Int. J. Adv. Curr. Pract. Mobil.* **2023**, *5*, 2078–2092. [CrossRef]
17. Saco, S.A.; Raj, R.T.K.; Karthikeyan, P. A study on scaled up proton exchange membrane fuel cell with various flow channels for optimizing power output by effective water management using numerical technique. *Energy* **2016**, *113*, 558–573. [CrossRef]
18. Shen, J.; Du, C.; Wu, D.; Yan, F. Experimental and numerical study of the enhancement effects on the performance of PEMFC with side blockage in straight flow-field. *Int. J. Hydrogen Energy* **2024**, *54*, 1231–1241. [CrossRef]
19. Brakni, O.; Kerkoub, Y.; Amrouche, F.; Mohammedi, A.; Ziari, Y.K. CFD investigation of the effect of flow field channel design based on constriction and enlargement configurations on PEMFC performance. *Fuel* **2024**, *357*, 129920. [CrossRef]
20. Zheng, D.; Liang, S.; Zhao, T.; Sun, L.; Fan, W.; Jiang, K.; Cui, H.; Yang, L.; Jia, S.; Lu, G.; et al. Bio-inspired sinusoidally-waved flow fields with exchange channels to enhance PEMFC performance. *Fuel* **2024**, *367*, 131552. [CrossRef]
21. Toghyani, S.; Atyabi, S.A.; Gao, X. Enhancing the specific power of a pem fuel cell powered uav with a novel bean-shaped flow field. *Energies* **2021**, *14*, 2494. [CrossRef]
22. Yuan, W.; Wang, A.; Ye, G.; Pan, B.; Tang, K.; Chen, H. Dynamic relationship between the CO_2 gas bubble behavior and the pressure drop characteristics in the anode flow field of an active liquid-feed direct methanol fuel cell. *Appl. Energy* **2017**, *188*, 431–443. [CrossRef]
23. Min, C.; He, J.; Wang, K.; Xie, L.; Yang, X. A comprehensive analysis of secondary flow effects on the performance of PEMFCs with modified serpentine flow fields. *Energy Convers. Manag.* **2019**, *180*, 1217–1224. [CrossRef]
24. Alizadeh, E.; Rahimi-Esbo, M.; Rahgoshay, S.; Saadat, S.; Khorshidian, M. Numerical and experimental investigation of cascade type serpentine flow field of reactant gases for improving performance of PEM fuel cell. *Int. J. Hydrogen Energy* **2017**, *42*, 14708–14724. [CrossRef]
25. Abdulla, S.; Patnaikuni, V.S. Enhanced cross-flow split serpentine flow field design for square cross-sectional polymer electrolyte membrane fuel cell. *Electrochim. Acta* **2021**, *391*, 138884. [CrossRef]
26. Sun, F.; Su, D.; Li, P.; Lin, F.; Miu, G.; Wan, Q.; Yin, Y. Effects of three-dimensional type flow fields on mass transfer and performance of proton exchange membrane fuel cell. *Energy* **2024**, *295*, 131111. [CrossRef]
27. Lu, K.; Zhang, J.; Ding, H.; Wang, Z.; Pan, X. Numerical and experimental investigation of 3D flow field bipolar plates for PEMFCs by metal 3D printing. *Fuel* **2024**, *357*, 129699. [CrossRef]
28. Edwards, H.; Pereira, M.P.; Gharaie, S.; Omrani, R.; Shabani, B. Computational fluid dynamics modelling of proton exchange membrane fuel cells: Accuracy and time efficiency. *Int. J. Hydrogen Energy* **2024**, *50*, 682–710. [CrossRef]

29. Bulgarini, M.; Della Torre, A.; Montenegro, G.; Baricci, A.; Grimaldi, A.; Mereu, R.; Marocco, L.; Collaku, A.; Savoldi, L. *Application of a CFD Methodology for the Design of PEM Fuel Cell at the Channel Scale*; SAE Technical Paper; SAE International: Warrendale, PA, USA, 2024. [CrossRef]

30. Weller, H.G.; Tabor, G.; Jasak, H.; Fureby, C. A tensorial approach to computational continuum mechanics using object-oriented techniques. *Comput. Phys.* **1998**, *12*, 620–631. [CrossRef]

31. Zago, M.; Baricci, A.; Bisello, A.; Jahnke, T.; Yu, H.; Maric, R.; Zelenay, P.; Casalegno, A. Experimental analysis of recoverable performance loss induced by platinum oxide formation at the polymer electrolyte membrane fuel cell cathode. *J. Power Sources* **2020**, *455*, 227990. [CrossRef]

32. Okonkwo, P.C.; Ige, O.O.; Barhoumi, E.M.; Uzoma, P.C.; Emori, W.; Benamor, A.; Abdullah, A.M. Platinum degradation mechanisms in proton exchange membrane fuel cell (PEMFC) system: A review. *Int. J. Hydrogen Energy* **2021**, *46*, 15850–15865. [CrossRef]

33. Zhang, S.; Hess, S.; Marschall, H.; Reimer, U.; Beale, S.; Lehnert, W. openFuelCell2: A new computational tool for fuel cells, electrolyzers, and other electrochemical devices and processes. *Comput. Phys. Commun.* **2024**, *298*, 109092. [CrossRef]

34. Andersson, M.; Beale, S.; Espinoza, M.; Wu, Z.; Lehnert, W. A review of cell-scale multiphase flow modeling, including water management, in polymer electrolyte fuel cells. *Appl. Energy* **2016**, *180*, 757–778. [CrossRef]

35. Beale, S.B. A Simple, Effective Viscosity Formulation for Turbulent Flow and Heat Transfer in Compact Heat Exchangers. *Heat Transf. Eng.* **2012**, *33*, 4–11. [CrossRef]

36. Beale, S.; Schwarz, D.; Malin, M.; Spalding, D. Two-phase flow and mass transfer within the diffusion layer of a polymer electrolyte membrane fuel cell. *Comput. Therm. Sci.* **2009**, *1*, 105–120. [CrossRef]

37. Udell, K.S. Heat transfer in porous media considering phase change and capillarity—The heat pipe effect. *Int. J. Heat Mass Transf.* **1985**, *28*, 485–495. [CrossRef]

38. Pasaogullari, U.; Wang, C. Liquid water transport in gas diffusion layer of polymer electrolyte fuel cells. *J. Electrochem. Soc.* **2004**, *151*, A399. [CrossRef]

39. Fuller, E.N.; Schettler, P.D.; Giddings, J.C. New method for prediction of binary gas-phase diffusion coefficients. *Ind. Eng. Chem.* **1966**, *58*, 18–27. [CrossRef]

40. Springer, T.E.; Zawodzinski, T.; Gottesfeld, S. Polymer electrolyte fuel cell model. *J. Electrochem. Soc.* **1991**, *138*, 2334. [CrossRef]

41. Goshtasbi, A.; García-Salaberri, P.; Chen, J.; Talukdar, K.; Sanchez, D.G.; Ersal, T. Through-the-membrane transient phenomena in PEM fuel cells: A modeling study. *J. Electrochem. Soc.* **2019**, *166*, F3154. [CrossRef]

42. Jomori, S.; Nonoyama, N.; Yoshida, T. Analysis and modeling of PEMFC degradation: Effect on oxygen transport. *J. Power Sources* **2012**, *215*, 18–27. [CrossRef]

43. Kongkanand, A.; Yarlagadda, V.; Gu, W.; Arisetty, S. Platinum surface oxide and oxygen reduction reaction kinetics during transient fuel cell operation. *J. Electrochem. Soc.* **2023**, *170*, 094506. [CrossRef]

44. Neyerlin, K.; Gu, W.; Jorne, J.; Gasteiger, H.A. Study of the exchange current density for the hydrogen oxidation and evolution reactions. *J. Electrochem. Soc.* **2007**, *154*, B631. [CrossRef]

45. Colombo, E.; Casadei, D.; Baricci, A.; Casalegno, A. An open-source zero-gradient cell hardware to improve and accelerate durability testing of PEM fuel cells. *HardwareX* **2023**, *16*, e00495. [CrossRef]

46. Bock, R.; Shum, A.; Xiao, X.; Karoliussen, H.; Seland, F.; Zenyuk, I.V.; Burheim, O.S. Thermal conductivity and compaction of GDL-MPL interfacial composite material. *J. Electrochem. Soc.* **2018**, *165*, F514. [CrossRef]

47. Grimaldi, A. Modelling and Experimental Analysis of Pem Fuel Cells under Dynamic Real-World Conditions Focusing on the Design of an Air Humidifier. Ph.D. Thesis, Politecnico di Milano, Milan, Italy, 2022.

48. Sarkezi-Selsky, P.; Schmies, H.; Latz, A.; Jahnke, T. Lattice Boltzmann simulation of liquid water transport in gas diffusion layers of proton exchange membrane fuel cells: Impact of gas diffusion layer and microporous layer degradation on effective transport properties. *J. Power Sources* **2023**, *556*, 232415. [CrossRef]

49. Shi, Y.; Janßen, H.; Lehnert, W. A transient behavior study of polymer electrolyte fuel cells with cyclic current profiles. *Energies* **2019**, *12*, 2370. [CrossRef]

50. Weber, N.; Knüpfer, L.; Beale, S.B.; Lehnert, W.; Reimer, U.; Zhang, S.; Ferreira-Aparicio, P.; Chaparro, A.M. Open-source computational model for polymer electrolyte fuel cells. *OpenFOAM® J.* **2023**, *3*, 26–48. [CrossRef]

51. Baricci, A.; Mereu, R.; Messaggi, M.; Zago, M.; Inzoli, F.; Casalegno, A. Application of computational fluid dynamics to the analysis of geometrical features in PEM fuel cells flow fields with the aid of impedance spectroscopy. *Appl. Energy* **2017**, *205*, 670–682. [CrossRef]